Journal of Marine Systems 255 (2026) 104209

Contents lists available at ScienceDirect

Journal of Marine Systems

journal homepage: www.elsevier.com/locate/jmarsys

The impact of windage on the transport and accumulation of marine litter: A Lagrangian analysis in the Bay of Biscay

S. Bertin [a,b,*], A. Rubio [b], I. Hernández-Carrasco [c,d], A. Orfila [c,e], A. Sentchev [a]

[a] Université du Littoral Côte d'Opale, Lab. of Oceanology and Geosciences (LOG), UMR 8187, Wimereux, France
[b] AZTI, Marine Research, Basque Research and Technology Alliance (BRTA), Pasaia, Gipuzkoa, Spain
[c] Instituto Mediterráneo de Estudios Avanzados (IMEDEA-CSIC-UIB), Esporles, Illes Balears, Spain
[d] Instituto de Ciencias del Mar de Andalucía (ICMAN-CSIC), Puerto Real, Spain
[e] School of Civil and Environmental Engineering, Cornell University, 14853 Ithaca, NY, USA

ARTICLE INFO

Keywords:
Coastal current convergence structures
Floating marine litter
Lagrangian diagnostics
Escape rates
Beaching
Coastal dynamics
High-frequency radar

ABSTRACT

The southeastern Bay of Biscay (SE-BoB) is known as an accumulation zone for marine litter. Coastal Current Convergence Structures (CCS), which are linked to vertical movements at the edges of river plumes, estuarine fronts, or other frontal processes, have been observed in this area to act as aggregators of floating marine litter (FML). Observed at the ocean surface, CCS often form narrow filament-like streaks with variable loads of FML. Understanding the role of CCS in the transport and aggregation of FML is crucial for quantifying and mitigating pollution. Within the Lagrangian framework, Finite Size Lyapunov Exponents (FSLE) and Finite Domain Lagrangian Divergence (FDLD) provide an effective way to identify and analyze CCSs in the area using velocity field data from the EuskOOS High-Frequency Radar network. Backwards-in-time FSLE and FDLD unveil Lagrangian Coherent Structures (LCS), which act as convergent transport barriers, a proxy of CCS where larger concentration of FML of different buoyancy is likely to occur. Since FML is buoyant and its motion can be driven also by windage, additional computations are conducted considering the effect of the wind drag force on FML trajectories and Lagrangian quantities. Escaping and beaching rate of particle clusters, delineating areas of different dynamic regimes, are also assessed considering different windage coefficients. Our results suggest that the wind has a significant influence on the FML distribution and accumulation paths in the study area, causing the aggregation of materials in areas not coinciding with CCS driven only by currents. Different locations of barriers to transport are obtained, depending on the wind regime and windage considered. Below 2–3% windage, aggregation structures are shifted in the direction of currents and winds. Above 3% windage, beaching and escaping rates are increasing and aggregation structures tend to merge.

1. Introduction

Coastal regions, defined as the transitional areas between land and open sea, are subjected to numerous anthropogenic pressures, mainly as the result of industrial activities, fishing or tourism. These regions are complex environments whose dynamics can evolve over a wide range of spatio-temporal scales. Different physical mechanisms, such as fronts and small eddies, control the transport of physical, chemical and biological substances (Nencioli et al., 2011; Zhang, 2017; Rubio et al., 2018). At the sub-mesoscale, with characteristic spatial scales less than 10 km, various physical processes drive current variability and generate fronts and eddy-like structures. These sub-mesoscale processes are known to be very important locally for the transport of passive quantities (McWilliams, 2016; Poje et al., 2014). Several mechanisms are responsible for the formation of kilometer-scale fronts, such as vertical movements at the edges of river plumes, estuarine fronts, or other frontal processes (Ayouche et al., 2020; Mann and Lazier, 2005). These small-scale fronts are associated with the intense convergence of horizontal flow induced by sub-mesoscale dynamics and can impact the distribution of buoyant material (D'Asaro et al., 2018; Hernández-Carrasco et al., 2018; Huntley et al., 2015). Sub-mesoscale surface ocean structures present a challenge to both numerical models and observations due to their chaotic nature and because high resolution is required to properly solve the related variability (Capó et al., 2021).

In the Lagrangian framework, quantities such as the Finite Size Lyapunov Exponent (FSLE) and Finite Domain Lagrangian Divergence

* Corresponding author at: 32 Avenue du Maréchal Foch, 62930, Wimereux, France.
E-mail address: sloane.bertin@gmail.com (S. Bertin).

https://doi.org/10.1016/j.jmarsys.2026.104209
Received 11 October 2024; Received in revised form 9 October 2025; Accepted 8 March 2026
Available online 17 March 2026

(FDLD) are very effective to unveil Lagrangian Coherent Structures (LCS) and to provide information on transport patterns associated with the flow, such as coherent convergence and divergence structures at the ocean surface (Haller, 2015; Hernández-Carrasco et al., 2018; Hernández-Carrasco and Orfila, 2018). Attracting LCS often coincide with Current Convergent Structures (CCS), where the accumulation of floating marine litter (FML) is likely to occur (Hernández-Carrasco et al., 2018; Huntley et al., 2015). However, FML is buoyant, and its motion can be driven also by windage, the additional direct wind-induced drift of material floating at the free surface of the ocean (also called wind-drift factor or leeway). Thus, relevant Lagrangian analysis metrics must account for this modified transport (Allshouse et al., 2017). In coastal ocean regions, the Lagrangian properties of the flow have been assessed using velocity data from models (Bertin et al., 2024b; de Mello et al., 2023; Kumar et al., 2023), from satellite altimetry (Siegelman et al., 2020), as well as from High-Frequency Radars (HFR) (Bertin et al., 2024a; Hernández-Carrasco et al., 2023; Tran et al., 2022; Veatch et al., 2022). The use of HFR technology has the potential to provide observational information with the necessary resolution in both space and time to unveil small scale structures such as CCS (Bertin et al., 2024a).

The southeastern Bay of Biscay (hereinafter SE-BoB) has been identified by global and regional models as an accumulation zone for marine litter (Pereiro et al., 2019; Rodríguez-Díaz et al., 2020). Previous studies on macrolitter (Ruiz et al., 2020) and microlitter (Davila et al., 2021), have shed a light on the quantities and behaviors of litter at the water surface in the SE-BoB, reinforcing the hypothesis of litter accumulation in the area. These recent studies also underscored the significant seasonal variability of this accumulation (Declerck et al., 2019; Pereiro et al., 2019; Ruiz et al., 2022). In a recent study in the area, Bertin et al. (2024a) have showcased the presence of CCS with FML loads, mostly associated with river plume edges, i.e. aligned with remotely sensed high concentrations of Chlorophyll-a, and in agreement with the in-situ observations made by Ruiz et al. (2020). Understanding the formation and evolution of the CCS and their role in the transport of FML is essential to better quantify and to help mitigate marine litter pollution. Bertin et al. (2024a) demonstrated that estimating FSLE from velocity data provided by HFR data allowed a realistic characterization of CCS, their location and evolution. The authors also reported the important role of the CCS in the accumulation of marine litter observed in windrows distributed alongshore, identified by filament-like structures of high FSLE values. However, the effect of windage on the computation of these CCS and on the precise detection of floating particle aggregation zones still remains unclear.

This paper focuses on the impact of wind on the transport of FML under different windage and on how wind affects the distribution and evolution of CCS driving the accumulation of FML in coastal waters of the SE-BoB. To do so, we use a combination of surface currents from drifters and HFR as well as realistic and theoretical modeled winds. The realistic winds are derived from a numerical model, while the theoretical winds represent constant regimes typical of the SE-BoB—namely north, northeast, northwest, and southwest winds (see Appendix B for details). Several simulations are performed taking into account a range of windage coefficients, representative of different types of FML (for example, a drifting container is subject to a windage of 1.4%, while a capped plastic bottle is subject to a windage of 4% (Breivik et al., 2011; Park and Seo, 2021)) and also accounting on FML from different provenance. We estimate beaching and escaping rates in the study area, aligned with absolute dispersion, FSLE and FDLD to showcase the impact of windage on the transport, fate and aggregation of FML.

The core of the article presents results obtained using realistic winds from an operational meteorological system. Additionally, four academic configurations, carried out using theoretical winds typical of the SE-BoB in the period of the observations, provide a detailed insight to the effect of wind variability on the structuration and transport of FML.

2. The southeastern Bay of Biscay

The study was conducted in the southeastern Bay of Biscay, spanning the region between northeastern Spain and southwestern France coasts. The study area extends from 43.27° to 44.58° N and from 3.18° to 1.27° W, falling within the coverage zone of the HFR system of the EuskOOS coastal operational observatory (Fig. 1). The geomorphology of the SE-BoB is marked at the Spanish coast by a narrow continental shelf and a steep slope, where the Capbreton submarine canyon stands out, reaching depths over 3000 m just a few miles from the coast. At the French side, the width of the continental shelf increases as we move towards the north. The wave climate in the SE-BoB is characterized by northwesterly swells generated by North Atlantic low-pressure systems, with strong seasonal variability—milder in summer due to the Azores anticyclone and highly energetic in winter (González et al., 2004).

The main current regime is dominated by the Iberian Poleward slope Current (hereinafter IPC), which is a surface-intensified, density-driven current that flows cyclonically along the continental slope of the area. The IPC, primarily driven by meridional temperature (density) gradients between southern and northern Atlantic waters, is modulated also by wind variability and depicts a strong seasonal variability (Charria et al., 2013; Rubio et al., 2019; Solabarrieta et al., 2014; Vandermeirsch et al., 2012).

In autumn and winter, the IPC has a relatively intense flow (20–50 cm/s at the surface), carrying warm waters from the southeastern corner of the Gulf northwards, resulting in a warm tongue stretching from the Basque country to Brittany. In spring and summer, the IPC weakens and becomes more variable, moving mainly eastwards (Charria et al., 2013; Rubio et al., 2019; Solabarrieta et al., 2014; Vandermeirsch et al., 2012). The interaction of the IPC with the abrupt bathymetry often generates eddies (e.g. Pingree and Le Cann, 1992).

On the continental shelf, circulation is mainly determined by wind variability (Fontán et al., 2009; González et al., 2004; Solabarrieta et al., 2015), and is strongly influenced by the orientation of the coastline. Thus, the effect of wind adds complexity to the seasonality (Rubio et al., 2018; Solabarrieta et al., 2015), with prevailing southwesterlies in autumn and winter (reinforcing the winter poleward flow), and northeasterlies in spring and summer (contributing to a weaker and highly variable equatorward flow). Transport and retention conditions at the surface vary at interannual, seasonal and even daily scales, influenced by the interplay of the aforementioned processes (Rubio et al., 2020). At shorter time-scales, the variability is dominated by tides, mainly semi-diurnal and weaker than in other areas of the Bay (Le Cann, 1990), and inertial waves (Rubio et al., 2011).

The most important freshwater influence on the SE-BoB shelf comes from the Adour River in France (Fig. 1b), with a mean annual discharge of 300 $m^3\ s^{-1}$ (Valencia et al., 2004). On the Spanish coast, the rivers have much lower discharges and are torrential in character, with very short time lags between rainfall and the resulting river flow. The main rivers draining the Spanish coast are the Nervión, Oria and Bidasoa (Fig. 1b), with average annual flows of 20 to 30 $m^3\ s^{-1}$ (Ferrer et al., 2009). The highest discharges are, in both cases, observed mainly in spring and autumn, while the lowest river flows occur in late summer.

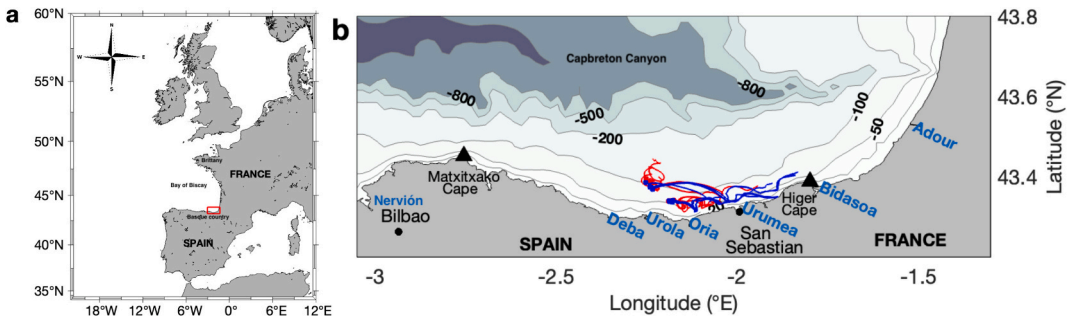

Fig. 1. Map of the study area. (a) Location of the study area as the red rectangle in the BoB. (b) Detailed map where the bathymetry is shown by blue shading and the black triangles display the location of the two HFR stations at Matxitxako (west) and Higer (east) Capes. The location of the major river mouths is given in blue. Trajectories of surface drifters with and without drogue are shown in red and blue, respectively. (For interpretation of the references to colour in this figure legend, the reader is referred to the web version of this article.)

3. Materials and methods

3.1. Lagrangian drifter surface current data

An in-situ experiment was conducted in the coastal waters of the SE-BoB during spring 2022, in an area where occurrence of coastal CCS was previously reported (BOBLIT0.1, see Bertin et al., 2024b, for more detail). From 26th April 11:45 UTC to 28th April 07:00 UTC, 20 surface drogued and undrogued drifters were deployed in pairs (pairing one drogued and one undrogued drifter) in two different clusters (centered at 43.4°N, −2.25°E and 43.35°N, −2.3°E, see Fig. 1b, red and blue dots for locations). In both clusters, the drifter pairs were deployed in areas within visible CCS and where qualitative aggregation of foam and macrolitter was observed (Bertin et al., 2024a). The mean separation distance between drifters was 1.7 and 0.6 km in the first and second cluster, respectively.

Regarding drogued drifters, three types of drifters were used: the coastal Nomad surface buoys, cylinder-shaped manufactured by SouthTek (https://www.southteksl.com/); ODI surface spherical buoys (not shown) formerly manufactured by Albatros Marine Technologies and a set of cylinder-shaped home-made drifters (whose design was similar to the coastal Nomad drifters (see Fig. 2a, b)). All drifters were equipped with a 0.5 m long drogue positioned in the water column between 0.8 and 1.3 m depth (Fig. 2c). It should be emphasized that the portion of the drifters exposed above the sea surface did not exceed 10 cm at wave troughs and was even smaller at wave crests, corresponding to less than 8% of the total drifter length. Most importantly, the presence of the drogue ensured that the drifter followed the surface currents rather than being influenced by wind drag, thereby making the current velocity measurements reliable.

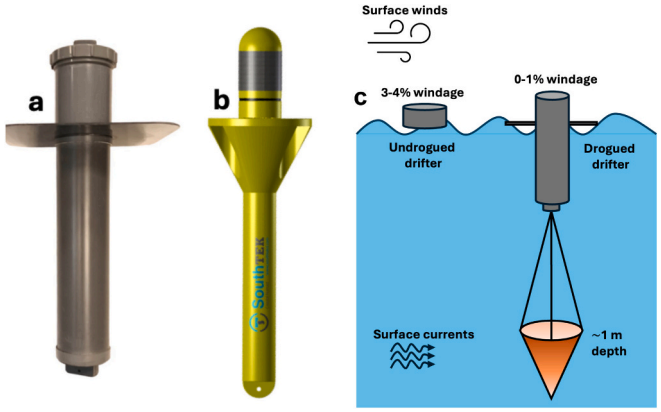

Fig. 2. Schematic of the drogued (a, b, c) and undrogued (c) drifters used during the survey and the windage to account for the impact of surface wind.

Undrogued drifters were home-made, featuring a plastic container of 9 cm in height and 9.5 cm in diameter, weighing approximately 200 g (see (Ruiz et al., 2022) for a detailed description and Fig. 2c for the schematic).

Observed surface current velocities were estimated from drogued and undrogued drifter trajectories with a timestep of 15 min, nominal period of drifter positioning via GPS. Potential differences in the behavior between different drogued drifter designs were neglected in the computation of Lagrangian diagnostics taking into account the short-term window considered (40 h) and that all drifters were equipped with the same drogues.

3.2. HFR surface current data

Hourly surface velocity current fields were obtained from a HFR system, consisting of two CODAR Seasonde stations situated along the Spanish Basque Country coast in the SE-BoB. The EuskOOS HFR system is part of euskoos observatory (https://doi.org/10.57762/T4WH-DQ48) and JERICO-RI (https://www.jerico-ri.eu/) and it is operated following JERICO standards and recommendations (Mantovani et al., 2020; Rubio et al., 2018; Solabarrieta et al., 2016). The two individual radar stations, operating at a frequency of 4.86 MHz, enable velocity measurements within the range of ~150 km with 5 km along-beam resolution, and 5° angular resolution. Velocity data are obtained at 1 h time step and distributed as part of Copernicus Global Ocean-in-situ near real-and delayed-time surface ocean currents products (http://doi.org/10.48670/moi-00041& http://doi.org/10.17882/86236).

Based on the measured radial velocities, refined surface current fields were generated using the two-dimensional variational interpolation method (2dVar) (Yaremchuk and Sentchev, 2009) covering an area between −3°E to −1.3°E and between 43.3°N to 44°N. The 2dVar technique enables to obtain hourly currents with 2.5 km spatial resolution. 2dVar is a non-local and kinematically constrained interpolation method which creates surface current velocity maps by using a combination of all measured velocities, within a given grid, reconstructing the velocity vector in one location. This interpolation technique has been used in a previous study in the SE-BoB and proved its reliability (see Bertin et al., 2024a, for detailed description).

3.3. Winds and windage computation

Wind velocity was obtained from the Weather Research and Forecasting model (WRF) provided by the Galician Meteorological Agency (Meteo Galicia). Hourly zonal and meridional components of wind velocity at a height of 10 m were used, featuring a spatial resolution of 4 km. Model details are given for completeness in Skamarock et al. (2019).

Windage refers to the drift induced by wind on floating objects, acting on the portion of the object above the water surface and can be estimated by a simplified model, following Yoon et al. (2009). In brief,

windage was computed at the surface as a fraction of the wind velocity at 10 m height:

$$U_{windage} = C_x U_{10} \tag{1}$$

$$U_T = U_{HFR} + U_{windage} \tag{2}$$

where $U_{windage}$ is the velocity of the drifter due to the wind, U_{10} is the wind speed at 10 m height, U_{HFR} the current velocity measured by HFR, and U_T is the total velocity. The wind drift factor C_x, depends on the geometry and the percentage of the emerged surface of the object (Sainte-Rose et al., 2016). This assumption considers a flat ocean surface, a purely downwind windage (symmetric object, no crosswind component) and wind velocities higher than both windage currents and oceanic currents. Stokes drift contribution to the total transport was not evaluated in this study; however, it is discussed in Section 5.

3.4. SOM clustering

Self-Organizing Map (SOM) clustering was used to obtain a map of different dynamical regions in the study area in order to seed particles in clusters for the analysis of escape rates and beaching. The SOM technique consists in an unsupervised learning neural network especially suited to extract nonlinear patterns in large datasets (Kohonen, 1998). This classification tool is used to map high-dimensional input data onto a two-dimensional space, while preserving the topological relationships between the input data (Liu et al., 2006). The input data are clustered in units, called neural units or neurons. The number of units is the same as the size of the SOM array (or lattice), where each unit has a weight vector that has the number of components equal to the dimension of the input sample data.

SOM learning process involves inputting velocity fields into a neural network, which undergoes modification through an iterative procedure. Each neuron is characterized by a weight vector, matching the dimensions of the input sample data. During each iteration, the neuron with the weight vector closest to the input data vector, identified by minimum Euclidean distance, is adjusted along with its neighboring neurons according to a specified neighborhood relationship defined by a mathematical function. By the end of the training process, SOM approximates the probability density function of the input data, assigning each neuron a reference pattern.

SOM clustering can be applied both in the spatial (e.g. Orfila et al., 2021) and temporal domains (e.g. Morales Márquez et al., 2021), according to the objectives of the study to be conducted. In this work, the SOM clustering was applied in the temporal domain in order to classify regions of the SE-BoB according to the temporal variability of surface currents measured by HFR. The input dataset consisted of a time series of three years of 2dVar HFR surface current velocities, which was normalized before starting the learning process and which included the land mask. The choice of the size of the neural network (i.e., the number of neurons) is not straightforward and depends on several factors: i) the number of samples; ii) the variability of the data; iii) the level of detail one wants to extract from the data, iv) the complexity of the patterns, as well as v) the need to minimize the quantization and the topographic error (Vatanen et al., 2015). A sensitivity analysis performed by Hernández-Carrasco and Orfila (2018) showed that using larger map sizes, for instance 8 × 8 (64 neurons) results in an unfeasible neural network because the large number of neurons does not allow the identification of clear patterns. The same happens with a 4 × 4 neural network: although the patterns are more detailed, the occurrence probability (OP), that is, the probability of finding a pattern similar to the input data, decreases, becoming zero in some cases, without improving the SOM analysis. Indeed, these additional neurons only split patterns into transitional patterns without sufficient significant occurrences. The opposite happens using a 2 × 2 neural network, where patterns are concentrated together with their occurrence probabilities in few rough patterns which increases, in this case, the topological error. In this work, since we are interested in analyzing the windage associated with the main patterns of velocity variability rather than fine-scale variability of the velocity field, we found that a map size of 2 × 3 neurons, (i.e 6 dynamical patterns and one of them associated with the land mask) provided the optimal representation of the main dynamical subregions in the study area. We used a rectangular map lattice and opted for a linear mode for the initialization, a batch algorithm for the training process, and an "gaussian" type of a neighborhood. The output of the analysis was a map of different sub-regions characterized with a particular temporal variability. The temporal patterns associated with each coherent region are presented in Appendix A.

3.5. Virtual particles advection and estimation of the L index

The potential impact of CCS and windage on the spatial distribution of FML was assessed by analyzing the trajectories of virtual particles advected in the 2dVar HFR velocity fields. Trajectories were computed with OpenDrift[1] code (Jones et al., 2016) and windage analyzed by imposing different windage coefficients. A 4th order Runge-Kutta scheme with a bilinear interpolation and a timestep of 1 h was used with no horizontal diffusion.

Virtual particle advection was used with three objectives: (i) to evaluate the reliability of surface current fields with different windage coefficients through the Lagrangian error, (ii) to estimate the rate of FML beaching and escaping the domain and (iii) to compute the PDF, FSLE and FDLD.

Considering d_{tk}, the separation distance between the real and the k-th simulated trajectory at time step t, the Lagrangian error was computed at each time step and averaged over all the simulated trajectories, following the expression:

$$\varepsilon_L(t) = \left\langle \sum_{t=1}^{N} \sum_{k=1}^{N-(t+1)} \frac{d_{tk}}{N-(t+1)} \right\rangle, \tag{4}$$

where N is the maximum number of time steps in the real trajectories. Simulated trajectories were launched at each time step of the real trajectories. Brackets indicate the average over all the simulated trajectories.

To facilitate comparisons, the Lagrangian error was divided by the mean drift distance D of the real drifters (travel distance averaged over all the drifters), giving rise to a dimensionless index: $L = \frac{\varepsilon_L}{D}$ (Bertin et al., 2024a, hereinafter L *index*).

To evaluate the rate of particles beaching on the French and Spanish coast and escaping from the northern and western parts of the domain, virtual particles were seeded and advected in dynamically distinct regions highlighted by the SOM clustering.

3.6. Lagrangian statistics

Absolute dispersion.

The absolute (cluster) dispersion $A^2(t)$ was used to quantify the intensity of the single-particle spreading induced by the surface current field. $A^2(t)$ is defined as the variance of particle spreading with respect to the barycenter of particles in a cluster. In two dimensions, the dispersion can be estimated along x and y axis following the expression (Berti et al., 2011; Enrile et al., 2019):

$$a_{ij}^2(t) = \frac{1}{M}\sum_{m=1}^{M}\left\{\left[x_i^m(t) - \underline{x_i^m(t)}\right]\left[x_j^m(t) - \underline{x_j^m(t)}\right]\right\}$$
$$A^2(t) = a_{xx}^2(t) + a_{yy}^2(t), \tag{6}$$

[1] https://opendrift.github.io/

where a_{ij}^2 corresponds to the variance along i and j spatial coordinates, a_{xx} and a_{yy} correspond to the absolute dispersion along x and y, respectively, M is the number of drifters, $x^m(t)$ is the position of the m-th drifter at time t and $\underline{x^m(t)}$ is the coordinate of the barycenter.

Estimating the absolute dispersion allows us to distinguish between fundamental dispersion regimes in a turbulent flow. At short timescales (i.e., during the initial hours of drifter deployment in coastal areas, more than 1 day in the open ocean), the absolute dispersion generally exhibits a ballistic growth pattern, following $A^2(t) \sim t^2$ (Berti et al., 2011; Bouzaiene et al., 2020; Davis, 1983; Enrile et al., 2019; Poulain and Niiler, 1989; Taylor, 1922). This regime is characterized by strong correlations in the velocities of drifter pairs, influenced by persistent and robust currents such as a coastal jet. Over longer timescales, when the influence of the initial conditions dissipates, the absolute dispersion tends to follow a random-walk regime, growing as $A^2(t) \sim t$.

Probability Density Functions.

To estimate the zones of intense passage of the virtual particles in the study region, the probability density function of the number of particles present in each grid cell during the simulation time were computed. This metric enables to unveil the most probable location of passage of particles and is calculated as follows:

$$PDF(i,j,t) = \sum_{i=1}^{N_i-1}\sum_{j=1}^{N_j-1}\sum_{k=1}^{N_k} Ind[x(ij)\, x(i+1j)\,] \\ (lon(tk)\,).Ind[y(ij)\, x(ij+1)\,](lat(tk)\,), \qquad (5)$$

where t corresponds to the time step, *lon* and *lat,* the longitudes and latitudes of the virtual particles, respectively. N_k corresponds to the total number of particles deployed during the simulation. N_i and N_j are the size of the grid in longitude and latitude, respectively, and x and y the longitude and latitude coordinates of the HFR grid, respectively. $Ind[a,b](x)$ is the indicator function of the interval $[a,b]$, which equals 1 if x is within the interval and 0 otherwise.

Finite-Size Lyapunov Exponents.

The study of turbulent transport and dispersion mechanisms can be approached by the characterization of the coherent structures in the flow field. The development of the coherent turbulent structures such as jets, eddies and fronts, is determined by the intrinsic spatial and temporal variability of the surface current field interacting with the external forcings (wind, waves and freshwater inflow, (Morales Márquez et al., 2023)). These dynamical structures dictate a large part of the transport characteristics (Haza et al., 2008).

The FSLEs help to identify these transport structures, providing information on velocity fluctuations and mixing in the marine flow (Aurell et al., 1997; d'Ovidio et al., 2004; Hernández-Carrasco et al., 2020; LaCasce, 2008). This method identifies the LCS that organize transport in a flow field, by locating regions of the flow that evolve on time scales different from the temporal variability of the surrounding field. Typically, these characteristic LCSs appear to be surrounded by lines of large FSLE values, also known as ridgelines (d'Ovidio et al., 2004; Hernández-Lasheras et al., 2025). As FSLEs cannot be crossed by particle trajectories, they act as barriers to transport, thus governing the movement of particles in the surrounding fluid flow around them. In this study, FSLEs are computed backward in time because, in these conditions, the resulting LCSs can be directly interpreted as attractive hyperbolic structures. Thus, they have a physical interpretation and can be used to identify CCS (Bertin et al., 2024a; Hernández-Carrasco et al., 2018).

FSLE values, denoted by λ, were estimated as the inverse of the time $\tau(x)$ required for two particles of fluid to separate from an initial distance δ_0 to a final distance δ_f, and is expressed at position $\boldsymbol{x}$ and time t as:

$$\lambda(x,t,\delta_0,\delta_f) = \frac{1}{\tau(x)} ln \frac{\delta_f}{\delta_0}. \qquad (7)$$

Values of λ were computed using the algorithm described in Hernández-Carrasco et al. (2011) with $\delta_0 = 0.4$ km and $\delta_f = 3.2$ km (amplification factor $\alpha = \delta_f/\delta_0 = 8$) in order to measure high stretching and obtain reliable attracting LCS. Particle trajectories were integrated backward-in-time over 10 days.

Finite-Domain Lagrangian Divergence.

FDLD computed backwards provides insights into flow regions that consistently exhibit persistent divergence or convergence in their Lagrangian motion, revealing coherent regions of flow divergence or convergence, which are associated with vertical dynamics. The deformation of an area (i.e. an infinitesimal fluid patch) can be described by the eigenvalues of the deformation gradient tensor. Accordingly, this area deformation is expressed as a combination of the stretch rate (ratio of the eigenvalues), which is area preserving, and the dilation rate (product of the eigenvalues), which is area changing. While the FSLE represents the material average of both the dilation and stretch rates, the Lagrangian-averaged divergence is related only to the dilation rate (Huntley et al., 2015), allowing to quantify flow deformation through area changes. Consequently, at the sea surface, high negative values of FDLD can be used as a physical proxy to identify regions of persistent flow contraction, where floating particles tend to aggregate, while attracting LCS highlights hyperbolic structures of intense fluid stretching, where particles are not only aggregated but also stirred or dispersed along filaments (Hernández-Carrasco et al., 2018). Thus, using these two metrics together enables the mapping of CCS, as shown in (Bertin et al., 2024a).

Assuming that the horizontal velocity field is divergent, the horizontal divergence ($\nabla_H.v$) can be computed along a particle trajectory $s(x_0,y_0,t_0)$ in the finite domain of the HFR coverage area at the sea surface. FDLD values were calculated by integrating or averaging horizontal divergence over fluid particle trajectories as follows:

$$FDLD(x_0,y_0,t_0,t_f) = \frac{1}{t_f - t_0}\int_{t_0}^{t_f} \nabla_H.v(x(t)\,,y(t)\,,t)dt, \qquad (8)$$

with $t_f - t_0$ the time interval of the trajectory integration and x_0 (resp. y_0) the initial longitude (resp. latitude) of the particle trajectory considered. Particle trajectories were integrated backward in time over 7 days, which corresponds to the duration of the shortest trajectory available from the deployment campaign as well as to the mean escape time averaged over the reduced HFR area of the 2dVar solution (see Rubio et al., 2020), and also because it is the time-scale associated with the dynamical features in this coastal region.

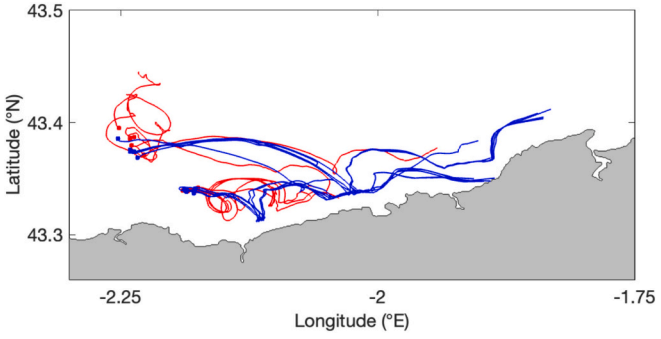

Fig. 3. Trajectories of surface drifters with drogue (red) and trajectories of surface drifters without drogue (blue) deployed from 26th April 11:45 UTC to 28th April 07:00 UTC. (For interpretation of the references to colour in this figure legend, the reader is referred to the web version of this article.)

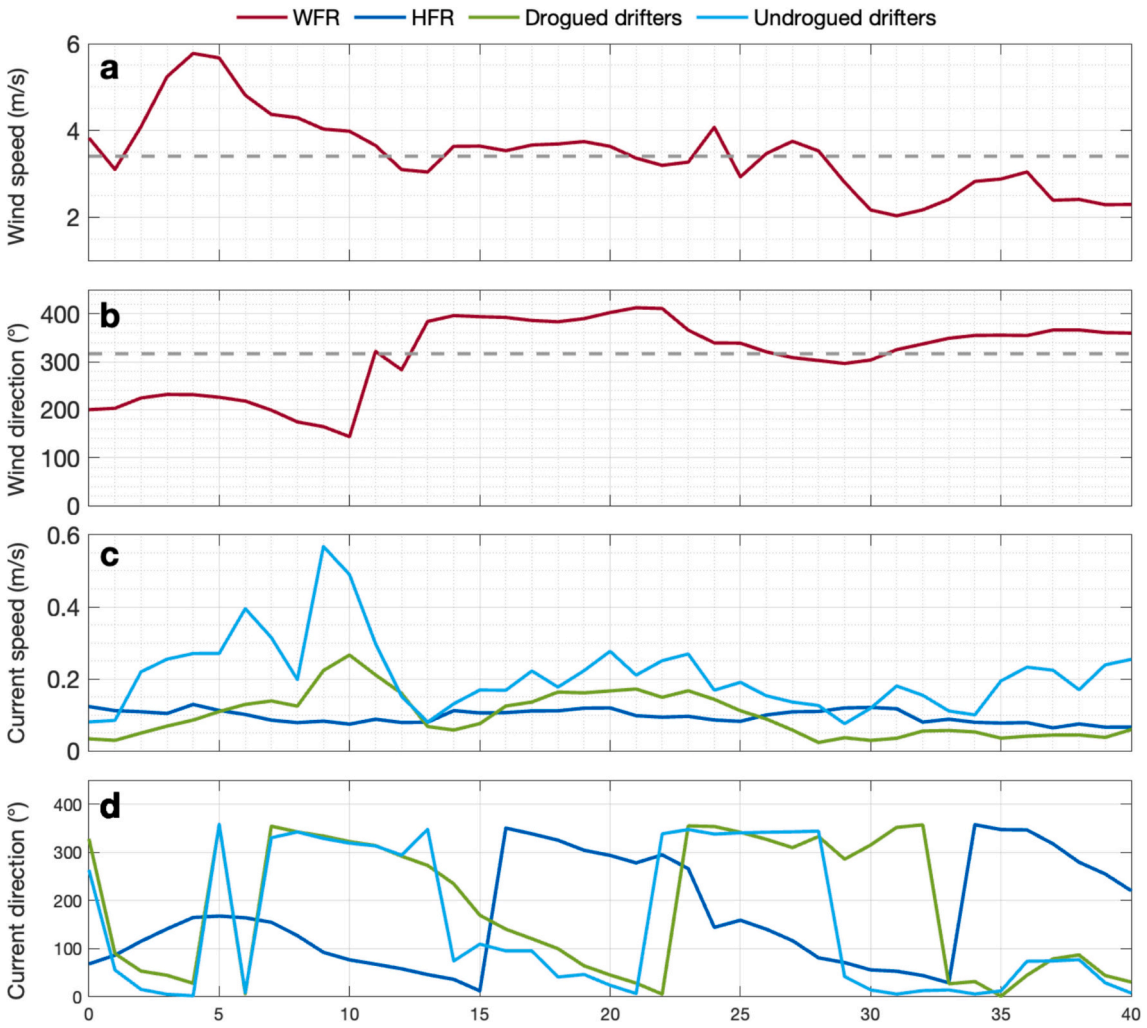

Fig. 4. Time series of (a) wind speed and (b) wind direction, spatially averaged over the study area, with dashed lines indicating the temporal mean of each variable. Panels (c) and (d) show surface current speed and direction, also spatially averaged over the study area, obtained from HFR measurements as well as from averaged drogued and undrogued drifter data.

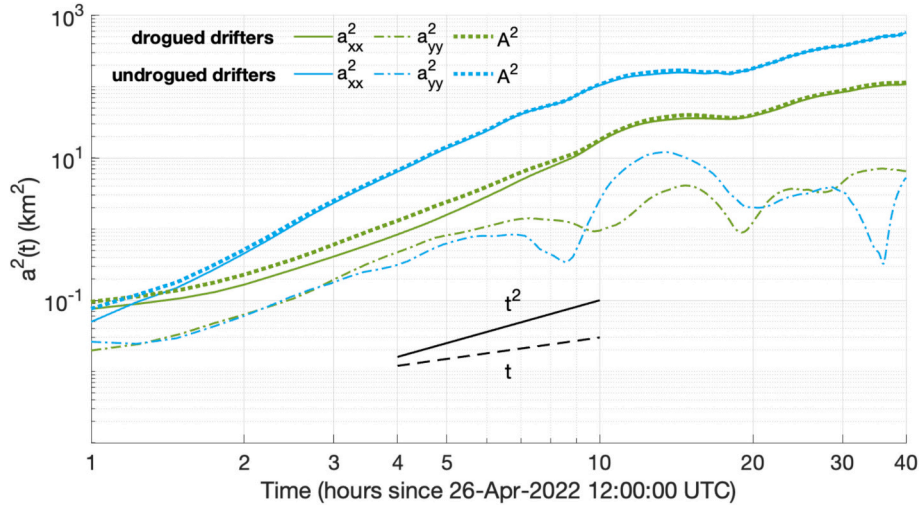

Fig. 5. Absolute dispersion considering drogued and undrogued drifters. The absolute dispersion along *x-axis (along-shelf)* is given in a solid line, the absolute dispersion along *y-axis (cross-shelf)* is given in a dashed line and the total absolute dispersion is given by the bold dot line. The ballistic (t^2) and diffusive (t) regimes are shown by solid and dashed black lines, respectively.

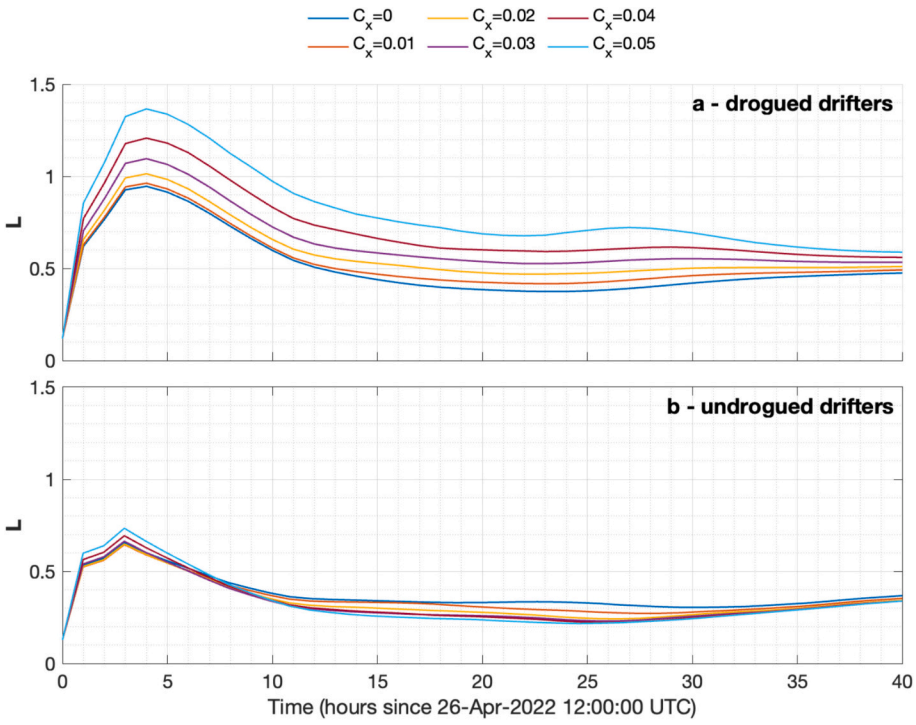

Fig. 6. L index computed with drogued drifters (a) and undrogued drifters (b) upon trajectories with various windage coefficient C_x.

4. Results

4.1. Trajectories of drogued and undrogued drifters

Drogued and undrogued drifter pairs trajectories are shown in Fig. 3. In the figure, we can observe the advection of the drifters predominantly towards the east, along the coast, with a marked difference in behavior between drogued and surface drifters. In general, the trajectories of the surface drifters cover greater distances and, although they exhibit some small-scale variability in the form of minor oscillations or vortices, their displacements are overall much faster. It is noteworthy that some of the drogued drifters in the cluster furthest from the coast show significant oscillations, with net movements towards the northeast of much smaller magnitude. To provide a qualitative description of the observed trajectories of the drifters in terms of mean speeds and directions and relate them to the time variability in wind and current conditions, Fig. 4 shows the time series of spatially averaged wind speed and direction, as well as the surface current speed and direction obtained from the numerical model and the HFR and drifters, respectively (see more details in Sections 3.2 and 3.3).

During the first ten hours of the trajectories, moderate winds (speed up to 5 m/s) from south-southwest were observed (Fig. 4a), while lighter winds (less than 3 m/s) from east-southeast (Fig. 4b) dominated afterwards. Mean surface current speed derived from HFR was around 0.10 m/s and exhibited very low temporal variability. Surface current predominant directions were more variable but in general towards the east-northeast (Fig. 4d). In contrast, the mean speed of undrogued drifters was twice larger (0.2 m/s) and exhibited a wider range of variability from 0.05 m/s to 0.60 m/s (Fig. 4c). Although Fig. 3 shows notable variability in the behavior of the different drifters inside each cluster (with and without drogue) this analysis of averaged velocities associated with the drifters reveals that, in general, there is a qualitative relation between the speeds and directions of the drogued buoys and the surface current, and between the undrogued buoys and the wind with a time shift of 5–6 h, and the highest drifting velocities being observed between the first 5 and 12 h (Fig. 4c).

Table 1
Mean *L* index for windage coefficients between 0 and 0.05 for both drogued and undrogued drifters. The lowest *L index* values are underlined.

	$C_x = 0$	$C_x = 0.01$	$C_x = 0.02$	$C_x = 0.03$	$C_x = 0.04$	$C_x = 0.05$
Drogued drifters	<u>0.52</u>	0.59	0.57	0.64	0.71	0.80
Undrogued drifters	0.39	0.36	0.34	<u>0.33</u>	0.34	0.34

Fig. 5 shows the absolute dispersion of real drifters along the *x* and *y* axes (aligned with along- and cross-shore directions). Both sets of drifters exhibit significantly greater dispersion along the *x*-axis. The dispersion along the x-axis is 16 times larger than along the y-axis for drogued drifters and 47 times larger for undrogued drifters. The difference in dispersion along the *x* and *y* axes is attributed to the shape of the Spanish coastline and the coastal jet, which generates a predominantly eastward along-shore transport. With only minor oscillations along the cross-shore *y*-axis, these results highlight a marked anisotropy in spreading. Additionally, the varying levels of mean dispersion between drogued and undrogued drifters can be explained by the windage effect.

Furthermore, the absolute dispersion, $A^2(t)$ is 5 times larger for undrogued drifters than for drogued drifters. Undrogued drifters experience an additional wind-induced velocity, leading to increased greater travel distances: 33.6 km for undrogued drifters and 19.4 km for drogued drifters.

Except for the difference in order of magnitude between the absolute dispersion of drogued and undrogued drifters, the dispersion regimes are similar. Indeed, during the first ten hours of the survey, the absolute dispersion of both types of drifters follows a ballistic regime characterized by $A^2(t) \sim t^2$ (Fig. 5). Subsequently, as the separation distance between drifters increases, the absolute dispersion transitions to a diffusive regime, characterized by $A^2(t) \sim t$.

Considering the significant differences in absolute dispersion experienced by drogued and undrogued drifters, it is useful to quantitatively determine the windage coefficient most suited to each type of drifter.

For this purpose, we use the Lagrangian error metric (L *index*), as detailed in section 3.5.

Thus, the calculation of the L index was performed by comparing real trajectories of drogued and undrogued drifters with those computed using surface currents and a varying wind-induced drag coefficient (from $C_x = 0$ to $C_x = 0.05$). Results are presented in Fig. 6 and Table 1, where we show the L *index* in time as well as its mean value through the study period. For drogued drifters, the lowest *L index* value (0.52) is obtained using $C_x = 0$. This is consistent because drogued Lagrangian drifter motions are designed to be driven solely by surface currents.

For undrogued drifters, the lowest *L index* value (0.33) is obtained for $C_x = 0.03$. This is consistent with the study by Ruiz et al. (2022), where they used the same surface drifters and obtained $C_x = 0.04$. The slight difference can be attributed to the different datasets used for the calculations (wind and surface currents).

The difference in the minimum absolute value of the L index obtained for drogued and undrogued drifters (0.52 for drogued drifters versus 0.33 for undrogued drifters) can be explained by the trajectory shapes of the undrogued drifters, which are more rectilinear and easier to resolve by the HFR than the oscillating trajectories of drogued drifters (Fig. 3).

These results further confirm the importance of accounting for windage effects when studying the transport of FML at sea. Depending on their shape, and particularly the area of emerging parts, different types of FML can exhibit significantly different trajectories, impacting on the absolute travel distances, pathways, beaching, preferential accumulation and escape rates.

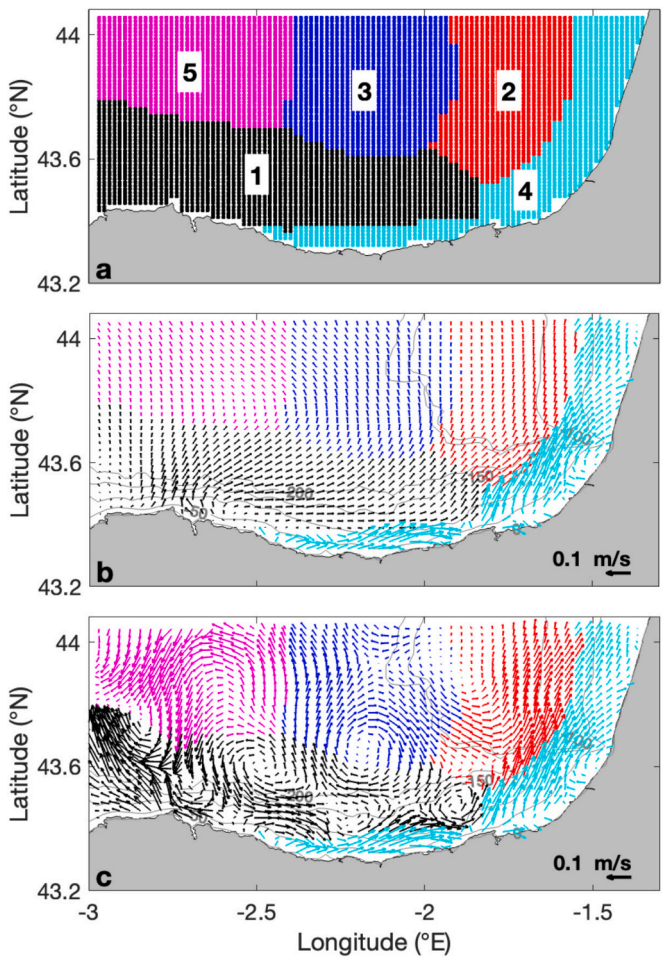

Fig. 7. Distinct dynamic regions revealed by the SOM clustering method, with the number of each region ranked in order of occurrence (a). Mean surface current velocity averaged over the 3-years of training data (b) and averaged over the survey period (c).

4.2. *Effect of wind on coastal circulation and transport*

Once we have characterized the range of windage coefficients associated with different objects exhibiting varying buoyancy and windage coefficients, in this section we examine, for the study period, how wind influences certain basic Lagrangian quantities, such as particle beaching along the coast and escape rates. To do this, we use the Lagrangian model, in which we release a number of particles classified according to the results of the SOM clustering of HFR velocity fields in the area, as explained in section 3.4 and using a range of windage coefficients. This allows us to analyze the effect of wind on the aforementioned basic Lagrangian quantities and to assess whether this effect differs significantly depending on the various regions of origin of the particles.

The SOM clustering enabled to unveil different coherent regions of similar velocity field variability. The SOM regions 1 and 2 (Fig. 7a in dark and red) correspond to the area of influence of the slope current (Rubio et al., 2019). SOM regions 3 and 5 correspond to regions where surface currents are weak and variable in direction due to the presence of eddies. SOM region 4 corresponds to the Region of Freshwater Influence (ROFI) (Reverdin et al., 2013). Placing this result in the context of marine litter, the regions provided by SOM clustering allows us to differentiate between particles representing FML that may originate from the coast —such as riverine litter resulting from river discharges or coastal activities—, in region 4, and debris coming from the western part of the study area (region 1) or entering from the north (region 2), which travels along the outer shelf and slope and may originate from discharges along remote western coastal zones. Particles in Cluster 5, in particular, would represent FML from open waters with an uncertain origin. Note that, the deployment locations of drifters during the survey are in region 4.

Fig. 7b shows the mean surface current velocity (averaged over three years), which reveals a significant coastal jet in SOM regions 1, 2, and 4. Low mean velocities are observed in drifters deployed in regions 3 and 5 (under 1 m/s), with an overall transport towards the north-northeast. Fig. 7c shows the mean surface current velocity observed by HFR during the survey, revealing weak variable currents and gyres in regions 1, 3, and 5 and a coastal jet which remains present and intense in regions 1, 2, and 4.

Virtual particles were deployed in all the study area and labelled using the five SOM regions (Fig. 7a). Particles were then advected with surface currents under various windage coefficients. A total of 5988 particles were deployed: 1768 in cluster 1 (SOM region 1), 976 in cluster 2 (SOM region 2), 1176 in cluster 3 (SOM region 4), 984 in cluster 4 (SOM region 4) and 1084 in cluster 5 (SOM region 5).

Fig. 8 presents the beaching rates in France and Spain, as well as the escape rates of virtual particles escaping north and west of the study area for different windages and considering realistic modeled winds during the field survey, i.e. 40 h including moderate winds from south-southwest in the first 10 h and mild winds from east-southeast in the following hours (Fig. 4a).

The beaching rates in France and Spain increase with windage, primarily due to contributions from cluster 4 in France and clusters 1 and 4 in Spain. The rate of virtual particles escaping from the western side of the study area also increases with windage up to $C_x = 0.04$, influenced by clusters 1 and 5, before decreasing from $C_x = 0.04$ to $C_x = 0.05$ due to the wind direction (east-southeast during most of the survey - Fig. 4b). Conversely, the rate of virtual particles escaping from the northern part of the study area decreases with increasing windage, whatever the origin of the particles. However, this decrease is less marked for region 4. The particles of region 4 escape from the northern part of the study area at similar rates for different windages. The decrease in the escape rates from the northern part of the study area for high windages may be influenced by the fact that under high windage a large number of the particles tends to beach either on the Spanish or French coasts.

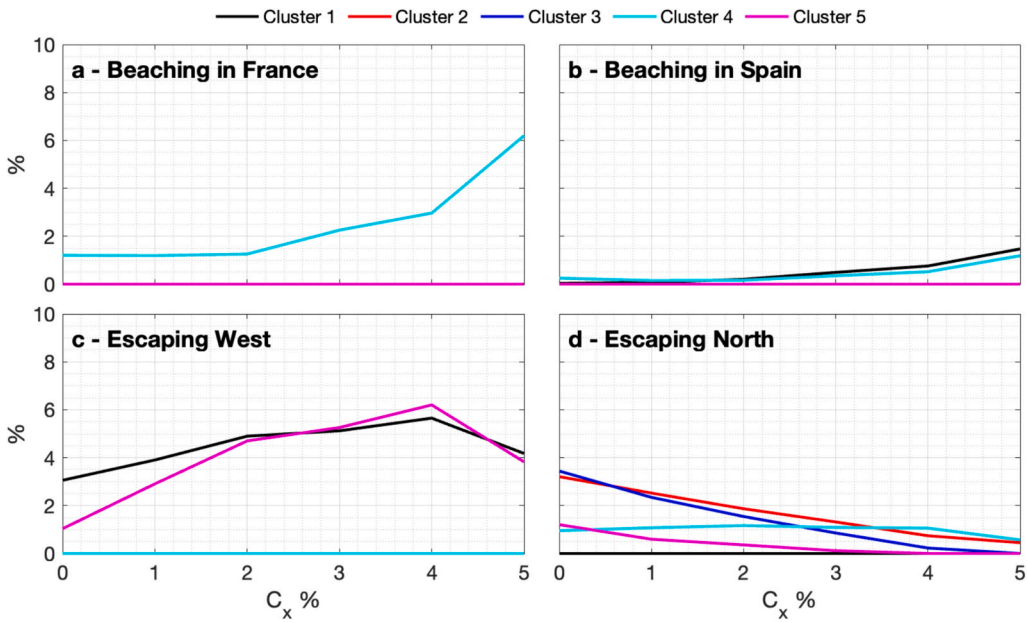

Fig. 8. Beaching and escaping rates of numerical particle clusters deployed in the five SOM regions shown in Fig. 7a, depending on the windage coefficient and considering realistic modeled winds during 40 h.

4.3. *Effect of windage on the coastal current convergence structures*

In addition to understanding how wind influences coastal particle accumulation and escape rates, in this section we analyze how particles aggregate at sea along convergence structures. To this end, we calculate FSLEs from a combination of surface currents and winds by using different windage coefficients. FSLE snapshots presented in Fig. 9 show that for $C_x = 0$, ridgelines are located parallel to the French and Spanish coasts, which is consistent with the alongshore filamental aggregation of FML observed in the study area (Ruiz et al., 2020).

When accounting for windage coefficients below $C_x = 0.03$, FSLE ridgelines remain present but are overall less defined, in accordance with the decrease in the FSLE mean values presented in Table 2 (0.51 days^{-1} for $C_x = 0$, and 0.47 days^{-1} for $C_x = 0.01$ and $C_x = 0.02$). The FSLE maximum values slightly increase with windage (Table 2 - from 2.29 days^{-1} with $C_x = 0$ to 2.43 days^{-1} with $C_x = 0.03$) but the region of maximum FSLEs is always located in the same area on the Spanish coast (i.e. -1.9°E, 43.4°N).

In contrast, above $C_x = 0.03$, FSLE ridgelines become less defined, and the thin filaments observed at $C_x = 0$ appear to merge at windages of $C_x = 0.04$ and $C_x = 0.05$, particularly on the French side of the study area. However, it also causes the disappearance of small-scale structures, especially on the French side of the domain, leading to a decrease in the FSLE maximum (Table 2 - from 2.43 days^{-1} at 3% windage to 1.59 days^{-1} at 5% windage). Although the spatial distributions of the main LCS are rather similar for different windage coefficients, new LCS emerge as C_x increases (i.e. in the central region) while other LCS disappear near the French coast.

The decrease in the number of FSLE ridgelines with higher windage is associated with increased beaching and escaping rates, but also with the fusion of ridgelines. As windage increases, the numerous convergent structures present in the study area (i.e. -1.6°E, 43.5°N) with $C_x = 0$ gradually merge into a single, wider structure. It is important to note that the disappearance of transport barriers and the easier passage of particulate matter are much more pronounced on the French side compared to the Spanish side, for the wind conditions corresponding to the integration time (10 days backwards in time).

Knowing that FSLE ridgelines structure the transport of particulate matter, FSLE values above 0.7 days^{-1} were superimposed on the PDF and FDLD fields. Snapshots are presented in Fig. 10 with PDF superimposed on FSLE (left panel) and FDLD superimposed on FSLE (right panel), only for $C_x = 0$, $C_x = 0.03$ and $C_x = 0.05$.

FSLE ridgelines align closely with the spatial distribution of PDF (Fig. 10, left panel), often surrounding areas with maximum values of PDFs. Maximum values of PDFs delineate areas of intense passage of virtual particles and are located in the northwest of the study region and close to the coast. These intense passage zones tend to be located in similar areas, regardless of the windage and wind direction considered, as presented in Appendix (Fig. B2). FSLE ridgelines also align closely with the ravines of FDLD, indicating significant gradients in the FDLD field (Fig. 10, right panel). Considering the windage effects, both the FSLE ridgelines and the areas with high values of PDF and FDLD ravines shift towards the northwest. Despite this shift, the FSLE ridgelines continue to align closely with the PDF and FDLD fields.

Additionally, a pronounced divergence alongshore is observed, which is consistent with the dominant coastal jet in the study region (Fig. 7b, c).

5. Discussion

Our results showcase how windage affects ocean surface transport, influencing the distribution and fate of FML in particular. Although these results are representative of a specific and limited period in the southeastern Bay of Biscay—where we have observational data—they provide valuable insight into the importance of selecting appropriate windage coefficients when performing Lagrangian simulations to study the origin, fate, or accumulation at open or coastal areas of FML with different characteristics and origin. The impact of windage is manifest in the varying fates and trajectories of virtual particles influenced by increasing windage. We suggest that wind-induced velocity plays a significant role in the behavior of FML transport and aggregation at the ocean surface. Although both drogued and undrogued drifters experience the same dispersion regime (a ballistic regime during the first ten hours of deployment, followed by a random-walk regime, as shown in Fig. 5), the magnitude of absolute dispersion for undrogued drifters is five times greater. Wind tends to increase both the absolute dispersion,

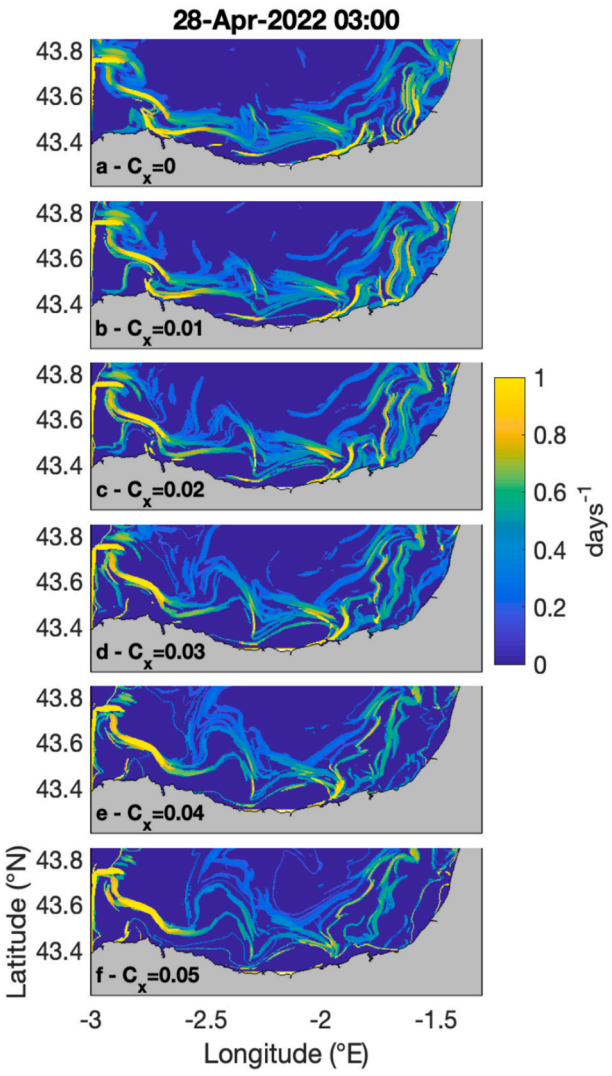

Fig. 9. FSLE snapshots under different windage coefficients and considering modeled realistic winds.

Table 2
FSLE maximum and mean (day^{-1}) for the snapshot (April 28th, 2022, 03:00) presented in Fig. 9.

	$C_x = 0$	$C_x = 0.01$	$C_x = 0.02$	$C_x = 0.03$	$C_x = 0.04$	$C_x = 0.05$
Max (day^{-1})	2.29	2.32	2.30	2.43	1.84	1.59
Mean (day^{-1})	0.51	0.47	0.47	0.49	0.50	0.51

and the distance traveled. Moreover, it significantly influences both the beaching and escape ratios and locations.

LCSs, provided by FSLE ridgelines, seem to act as transport barriers for FML, as evidenced by the distribution of high values in the PDF fields aligned with FSLE ridgelines. Moreover, high coherence is observed between the FSLE ridgelines, FDLD and transport patterns for different windages, with a pronounced divergence alongshore in the studied period for the conditions of the experiment. Allshouse et al. (2017) were the first to assess the impact of windage on LCS. They demonstrated that the windage was influencing the transport of material patches by altering their initial positions and the arrangement of strainlines around Lagrangian hyperbolic saddle-points. Windage shifts and reshapes these structures rather than creating or destroying them, which is crucial for interpreting ocean transport dynamics. The calculation of FSLE and FDLD with surface currents and wind, using different windage coefficients, demonstrated the effect of wind in CCSs location and intensity. This result underlines that the trajectories of different types of FML, submitted to different windage, are subject to different barriers to transport, depending on the wind drag they experience along their trajectory. However, the accurate implementation of the combined effect of currents and wind in the computation of transport is challenging, since it relies heavily on the quality of surface velocity and wind field data (Bertin et al., 2024b, 2024a). The use of drifters and HFR radar data have proven to provide good approximation to LCSs for the period analyzed, but the characterization of transport and aggregation paths along seasonal or interannual periods would require longer and reliable data sets. The progress in improving coastal models through atmosphere ocean coupling, the implementation of real time riverine runoff, and multi-platform data assimilations (including HFR data) or the use of data blending techniques is a key element towards accurate monitoring and forecasting of FML hotspots in the coastal ocean.

In this study, we estimated the impact of windage on the transport of FML using realistic surface winds. However, the results are only representative for the specific conditions during the analyzed period. In order to discuss the effect of wind from different directions in the study areas and the surface current conditions of the specific period analyzed, we have also computed escape rates, beaching and Lagrangian quantities under different theoretical wind patterns dominant in the study area. The results of these calculations are presented in Appendix B, and Table 3 presents the conclusions compared to those obtained with realistic winds.

Results in Table 3 show that winds from the north (N, NE and NW) are the least favorable for particle evacuation in the area as they lead to a decrease in escape through the northern border (also the western border, in the case of north-westerly winds) and are the most favorable for beaching on the Spanish coast. South-westerly winds increase escape through the northern border but also increase beaching on the French coast. The impact of different wind directions on FSLE, FDLD, and PDF can be summarized by a shift in the locations of LCSs and regions of higher passage, in the direction of the prevailing winds. In general, we observe no significant changes in the number of observed LCSs or areas of intense passage for most of the cases, excepting the area off the French coast where the number of LCS drastically decreases with north-westerly winds. North-westerly winds have the worst impact in the area, inducing a decrease in escape through both the northern and western borders and an increase in beaching on both the French and Spanish coasts. These results highlight the importance of this type of analysis to provide a basis for planning cleanup or mitigation strategies to face the issue of pollution by FML. The aggregation of FML along LCSs is crucial for active fishing for litter activities which would be extremely inefficient otherwise, as discussed in (Ruiz et al., 2020). To understand the complex distribution of FML due to the effect of LCSs is also important for the interpretation and planning of future sampling surveys aiming to quantify and map this pollution at the sea. The presence of submesoscale LCSs is also relevant for other types of particles and passive tracers, thus our results may have other applications related to ocean biogeochemical cycles or marine biology.

In addition to wind drag, another process which may have a significant effect on the transport of passive particles in the coastal area is the Stokes drift—the wave averaged difference between the mean Lagrangian velocity of a fluid parcel and the mean Eulerian velocity given at a fixed location. Previous works indicate that this additional

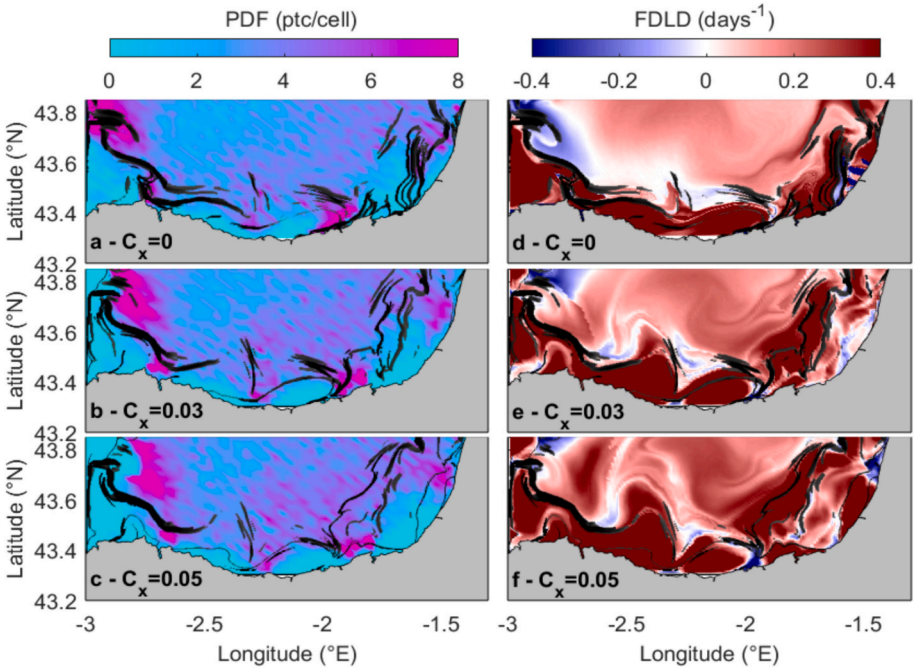

Fig. 10. PDF snapshots on April 28th, 2022, at 03:00 with superimposed FSLE ridgelines (a, b, c) and FDLD snapshots on the same date with superimposed FSLE ridgelines (d, e, f). The FSLE ridgelines have been plotted above the threshold of 0.7.

Table 3
Summary of impacts under the surface current conditions of the study period of different wind directions with increasing windage on the beaching, escaping rates, PDFs, FSLE and FDLD compared with those for WRF realistic winds. Conclusions about escaping and beaching rates are based on Figs. 8 for WRF winds and B3 for theoretical winds. Conclusions about the FSLE and FDLD are based on Figs. 9 and 10 for WRF winds, and Figs. B4 and B5 for theoretical winds. Conclusions about PDF are based on Fig. B2.

	WRF winds	N winds	NE winds	NW winds	SW winds
Escaping N	Decreasing with windage	Decreasing with windage	Slightly decreasing with windage	Decreasing with windage	Increasing with windage
Escaping W	Increasing with windage under 4%, then decreasing	Constant with windage	Increasing with windage	Decreasing with windage	Decreasing with windage
Beaching F	Increasing with windage	Increasing with windage	Decreasing with windage	Increasing with windage	Increasing with windage
Beaching S	Slightly increasing with windage	Increasing with windage	Increasing with windage	Increasing with windage	Slightly decreasing with windage
FSLE & FDLD	- Displacement towards north-west under 3% windage - Fusion of LCS and less structures observed above 3% windage	- Displacement towards south under 3% windage - Fusion of LCS and less structures observed above 3% windage on the French side	- Displacement towards south-west under 3% windage - Fusion of LCS and less structures observed for 3–4% windage	- Displacement towards south-east under 3% windage - Fusion of LCS observed above 3% windage on the Spanish side - Less LCS observed on the French side	- Displacement towards north under 3% windage - Fusion of LCS and less structures observed above 3% windage
PDF	- Intense passage zone located in the same areas under 3% windage, vanishing above 3% windage	Intense passage zones located in similar areas regardless of windage	Intense passage zones slightly shifted towards west with increasing windage	Intense passage zones located in similar areas regardless of windage	Intense passage zones shifted towards north-east with increasing windage

velocity can significantly alter the transport pathways of passively advected particles (Curcic et al., 2016; Dobler et al., 2019; Morales Márquez et al., 2023; van den Bremer and Breivik, 2018). Stokes drift is estimated to be about 1% of the wind speed (Ardhuin et al., 2018; Ardhuin et al., 2012). The inclusion of Stokes drift in HFR measurements remains contentious. Some studies argue that HFR systems do not measure Stokes drift (Röhrs et al., 2015; van den Bremer and Breivik, 2018), while others disagree (Ardhuin et al., 2009; Chavanne, 2018; Dussol et al., 2022). However, (Breivik and Allen, 2008) showed that transfer of energy associated with wave forces to small floating objects (i.e., less than 30 m) decay rapidly as the ratio of the dominant wavelength of the incident wave to the drifting object's length increases. These forces become negligible compared to wind forces when the wavelength is approximately six times larger than the size of the floating object (Hodgins and Hodgins, 1998; Mei, 1989). On the other hand, previous works have shown that big swells largely impact on the surface circulation and transport patterns (see Morales-Marquez et al., 2021, 2023), and for the target period analyzed here, mean significant wave height was over 1 m (source euskoos.eus), so we expect a significant contribution of Stokes drift to the transport of FML. However, this work focuses on assessing the effect of wind (mainly windage) on the transport properties, particularly on the formation of aggregation structures in coastal areas. The role of wave-induced dynamics in particle accumulation should be addressed in a separate, dedicated study.

Furthermore, the effect of Stokes drift could be significant in other periods and study areas with high exposure to energetic waves and deserves further attention in a dedicated future work. Lagrangian simulations performed in this work have also some limitations which could be improved in future works, such as more accurate beaching parameterization and more realistic behaviors of particles at the open boundaries (for instance, allowing particles escaping through the open boundaries to reenter the domain under favorable conditions).

Perspectives inherent to this study are to focus on the three-dimensional aspects of the CCS. Current convergence and divergence processes are closely linked to vertical movements, which can impact the distribution of particulate matter in the water column. Submesoscale structures are associated with horizontal density gradients (i. e., frontal zones) with strong surface convergence and water subduction. These structures can easily generate a three-dimensional distribution of material initially drifting to the surface (D'Asaro et al., 2018; Essink, 2019). Understanding these three-dimensional transport structures is crucial, as they control the Lagrangian connectivity between the upper ocean and deeper layers, inducing and effective vertical mixing. These flow structures control the supply of nutrients necessary for the growth of marine organisms, impacting the fate of many biogeochemical variables (Gove et al., 2019). On the other hand, toxic materials such as hydrocarbons or marine waste, accidentally spilled at sea, can be carried to depth by downward movements, amplifying their impact on the ecosystem (Cózar et al., 2014; D'Asaro et al., 2018). Plastic waste, in particular, is subject to biofouling (the accumulation of microorganisms, plants, algae and animals on submerged structures) and tends to fragment, increasing its presence in the water column (Lobelle et al., 2021). In the SE-BoB, samplings were performed in coastal CCS enabling the gathering of 16.2 tons of FML where plastic was the predominant material, making up 96% of the items collected (Ruiz et al., 2020). Thus, the three-dimensional aspect of coastal CCS is an area for further study. In addition, Lagrangian diagnostics such as FSLE and FDLD, which have proven their worth in identifying surface current convergence structures, can also be used to infer three-dimensional LCS and the impact of the vertical dynamics on the transported particles, such as plastics, organisms, etc. (Bettencourt et al., 2013; Taani et al., 2019).

6. Conclusion

Our analysis provides insight into the impact of windage on FML transport and accumulation in coastal environments. For the specific period analyzed here, when windage is below 2–3%, the aggregation structures of FML are primarily generated by the combined effect of ocean currents and prevailing winds. In contrast, when windage exceeds 3%, we observe a marked increase in beaching events and escaping rates of FML, accompanied by a reduction in the number of relevant aggregation structures. Despite variations in wind direction, the zones with high FML concentration tend to be located in the same areas. The origin of the FML loads found within these aggregation zones can vary depending on the specific characteristics of FML items and their exposure to windage, suggesting the importance of accurately accounting for the interplay between windage and surface currents when using Lagrangian analysis tools to study FML transport. Lagrangia techniques, such as FSLE and FDLD prove to be invaluable for identifying CCS and elucidating the transport pathways of FML. Although these results are representative of a specific and limited period in the southeastern Bay of Biscay, they provide valuable insights into the importance of selecting appropriate windage coefficients when performing Lagrangian simulations to study the origin, fate, or accumulation of FML with different characteristics and origin in open or coastal areas. Such improvements could significantly enhance coastal management practices, providing a clearer understanding of the underlying transport structures and ultimately leading to more informed decisions in managing coastal and estuarine environments.

CRediT authorship contribution statement

S. Bertin: Writing – original draft, Methodology, Investigation, Formal analysis, Conceptualization. **A. Rubio:** Writing – review & editing, Supervision, Project administration, Methodology, Investigation, Funding acquisition, Formal analysis, Conceptualization. **I. Hernández-Carrasco:** Writing – review & editing, Formal analysis, Conceptualization. **A. Orfila:** Writing – review & editing, Formal analysis, Conceptualization. **A. Sentchev:** Writing – review & editing, Supervision, Methodology, Investigation, Funding acquisition, Formal analysis, Conceptualization.

Declaration of competing interest

The authors declare no competing interests.

Acknowledgements

The Ph.D thesis of Sloane Bertin has been co-funded by the Region Nord-Pas de Calais, Université du Littoral Côte d'Opale and AZTI Foundation. This work is part of the Graduate school IFSEA that benefits from grant ANR-21-EXES-0011 operated by the French National Research Agency, under France 2030 program. Authors acknowledge financial support from the French National program LEFE (Les Enveloppes Fluides de l'Environnement) and the Spanish LAMARCA project (PID2021-123352OB-C31, C33) and the project COPLA (PID2023-153236NA-I00) both funded by MCIN/AEI/10.13039/501100011033 and by ERDF A way of making Europe as well as from #ebegi project, funded by the Directorate of Agriculture, Fisheries, and Food Policy of the Department of Economic Development, Sustainability, and Environment of the Basque Government. We thank the Emergencies and Meteorology Directorate (Security department) of the Basque Government for public data provision from the Basque Operational Oceanography System EuskOOS. This study has been conducted using EU Copernicus Marine Service information. Wind data were obtained from the meteorological agency of Galicia (MeteoGalicia). The processing of HFR data was supported by the JERICO-S3 project, funded by the European Union's Horizon 2020 Research and Innovation Program under grant agreement no. 871153. The authors gratefully thank all people who gave their time and expertise in this study, especially E. Lecuyer for creating the home-made drifters, O.C. Basurko for her work in the design and execution of the BOBLIT surveys, I. Lizarán and B. Casas (SOCIB) for providing the ODV drifters and P. Losa and EKOCEAN crew for their support and availability during the BOBLIT surveys. The present research was carried out in the framework of the AEI accreditation "Maria de Maeztu Centre of Excellence" given to IMEDEA (CSIC-UIB) (CEX2021-001198). This paper is contribution nº 1304 from AZTI, Marine Research, Basque Research and Technology Alliance (BRTA).

Appendix A. Temporal patterns of SOM clusters

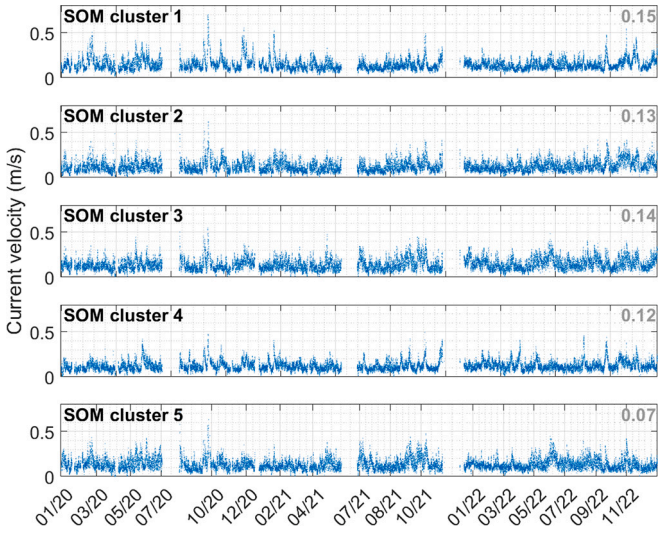

Figure A. Temporal patterns of surface current velocity associated with each coherent region during the 3 years of SOM training. The mean velocity is shown in gray at the top right of each figure.

Appendix B. Theoretical wind regimes

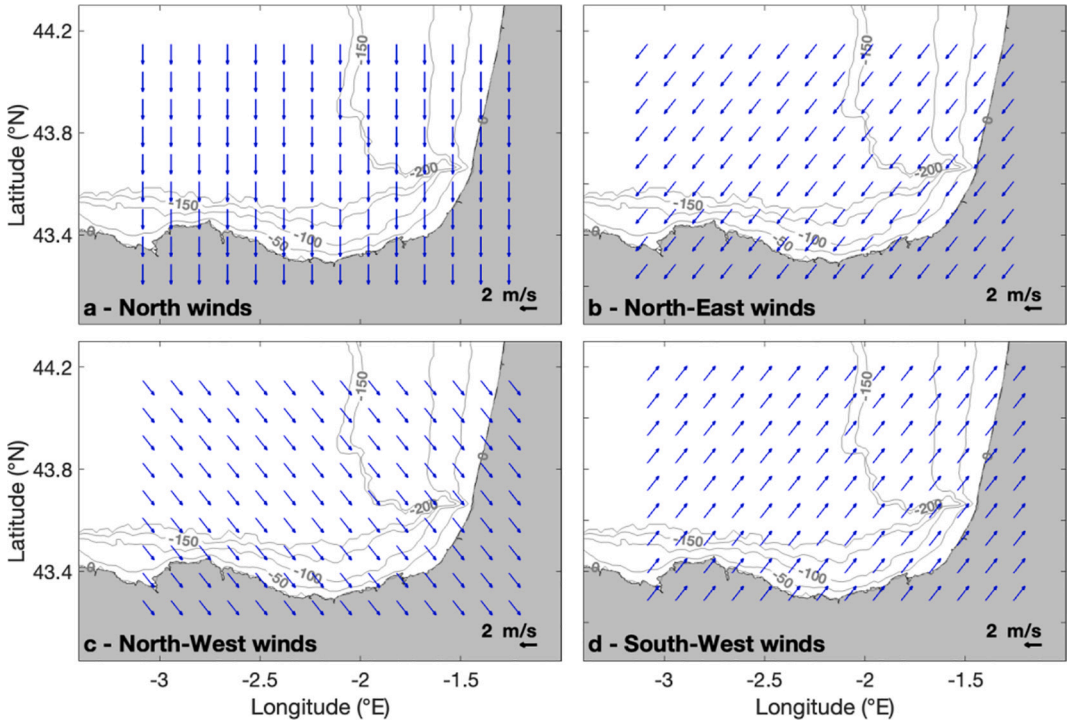

Fig. B1. Four theoretical wind regimes used in the computation of surface current fields with windage used to estimate escaping and beaching rates, PDF, FDLD and FSLE fields.

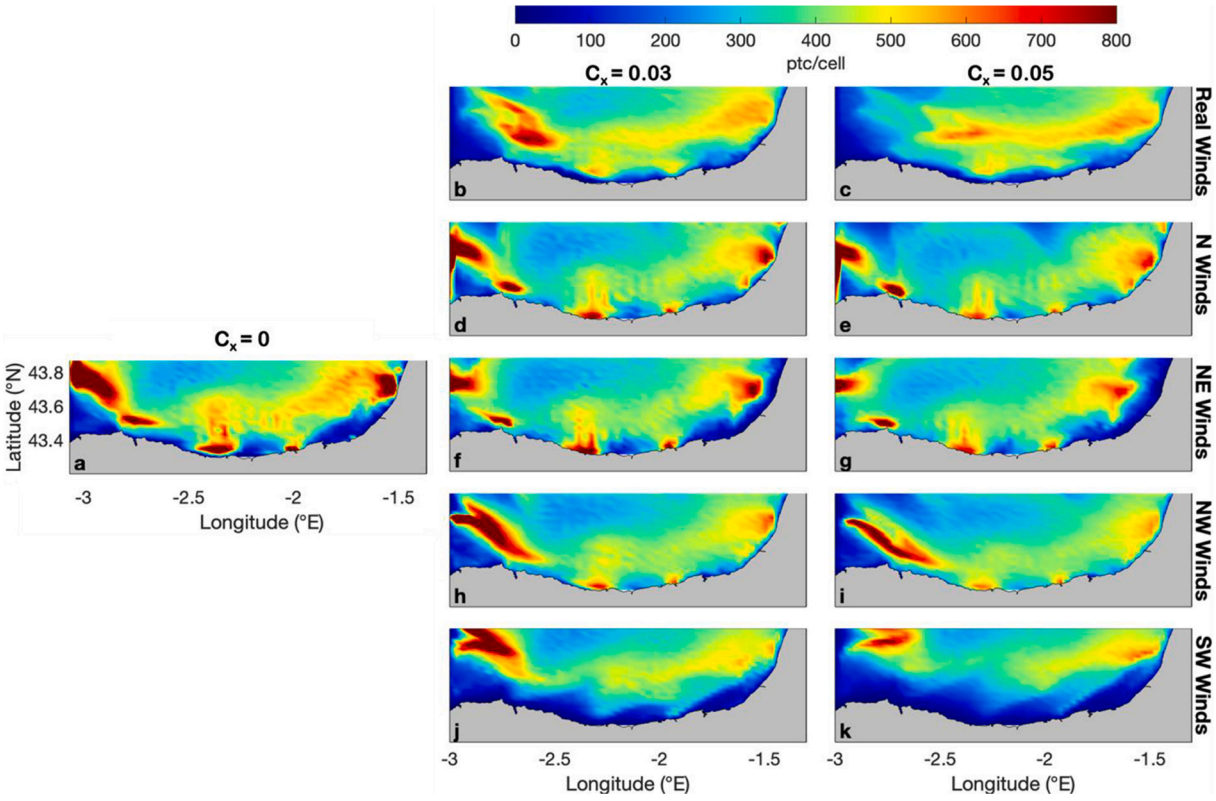

Fig. B2. Summed PDF for the different theoretical wind directions and for a windage of 0% (left panel), 3% (middle panel) and 5% (right panel).

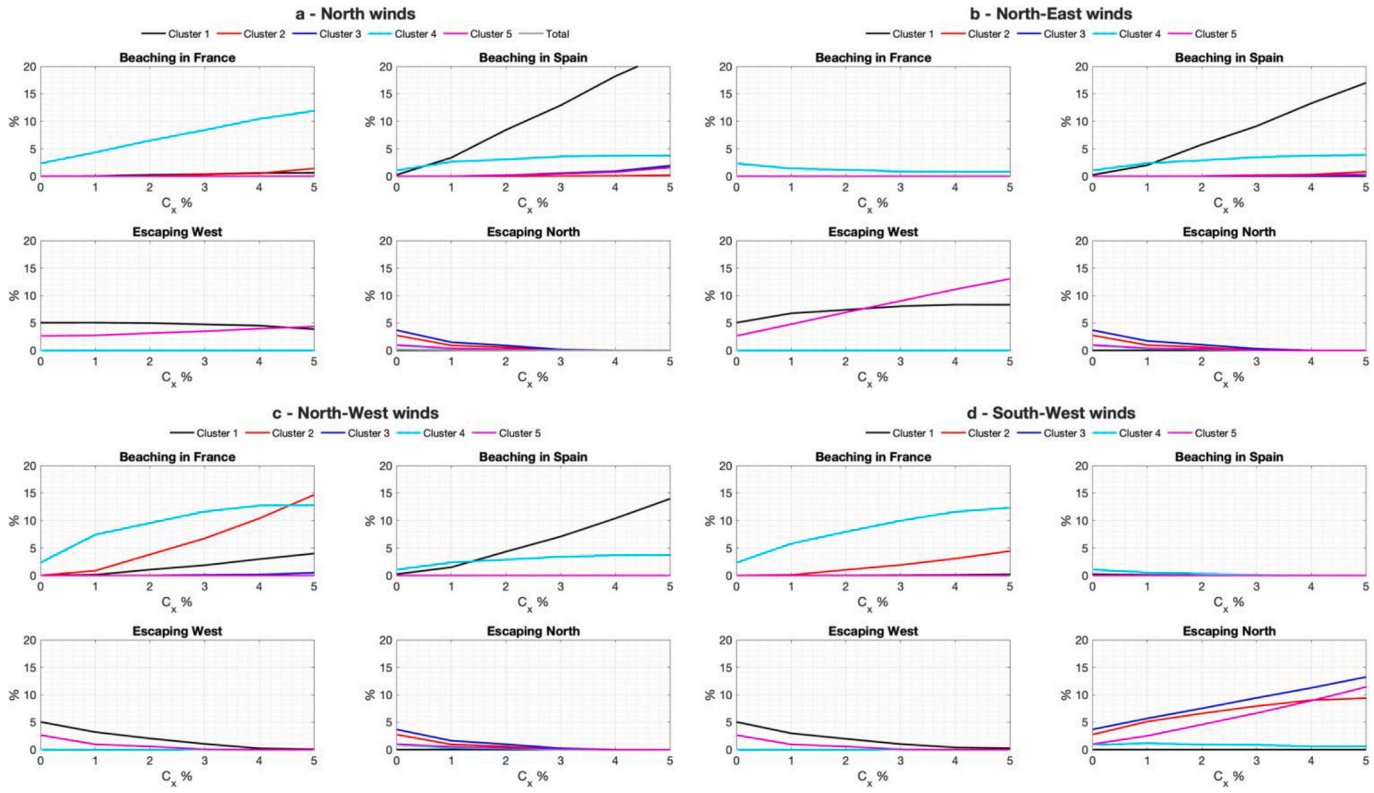

Fig. B3. Beaching and escaping rates depending on the windage coefficient and the theoretical wind direction.

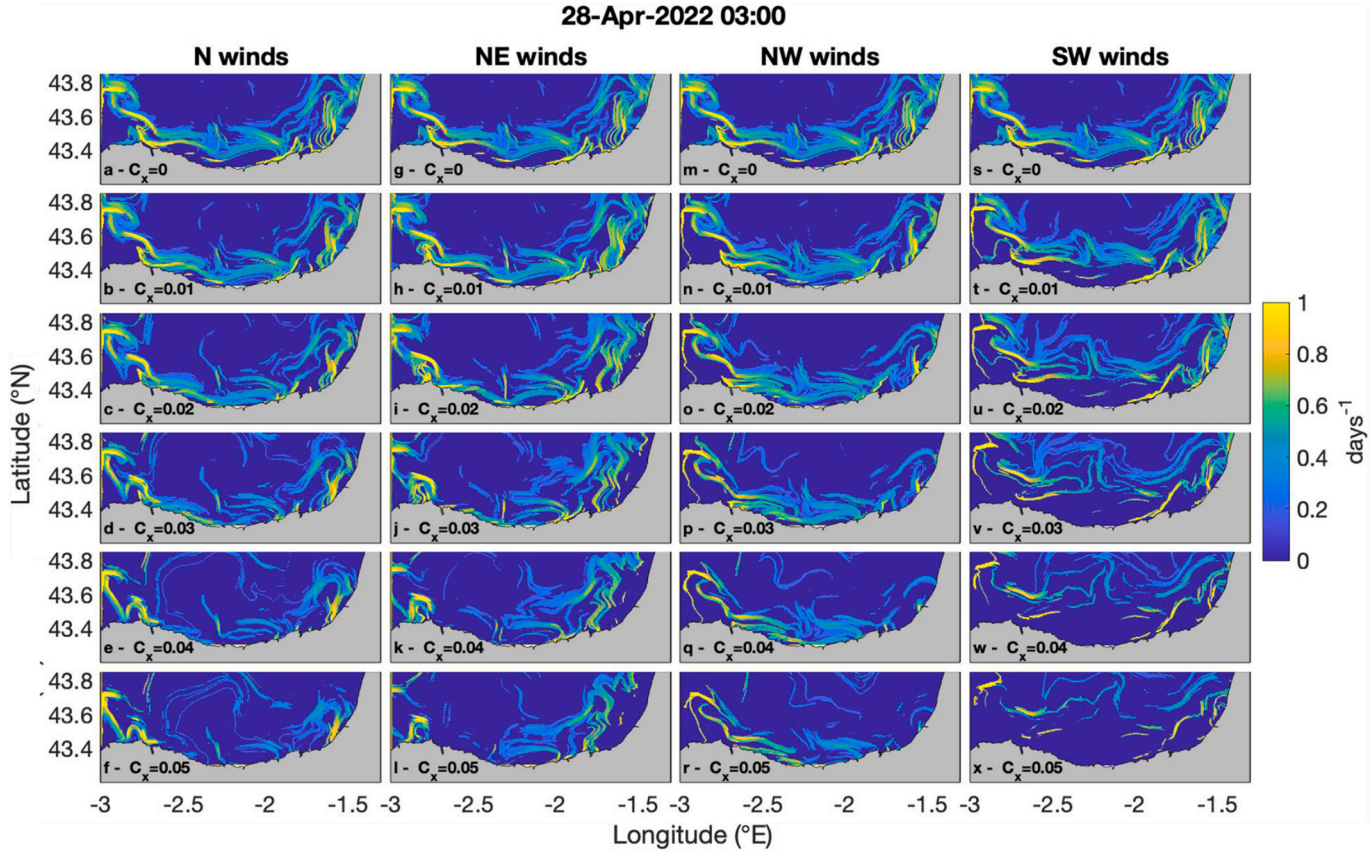

Fig. B4. FSLE snapshots computed with the 2dVar HF radar fields with different windage coefficients considering four theoretical winds.

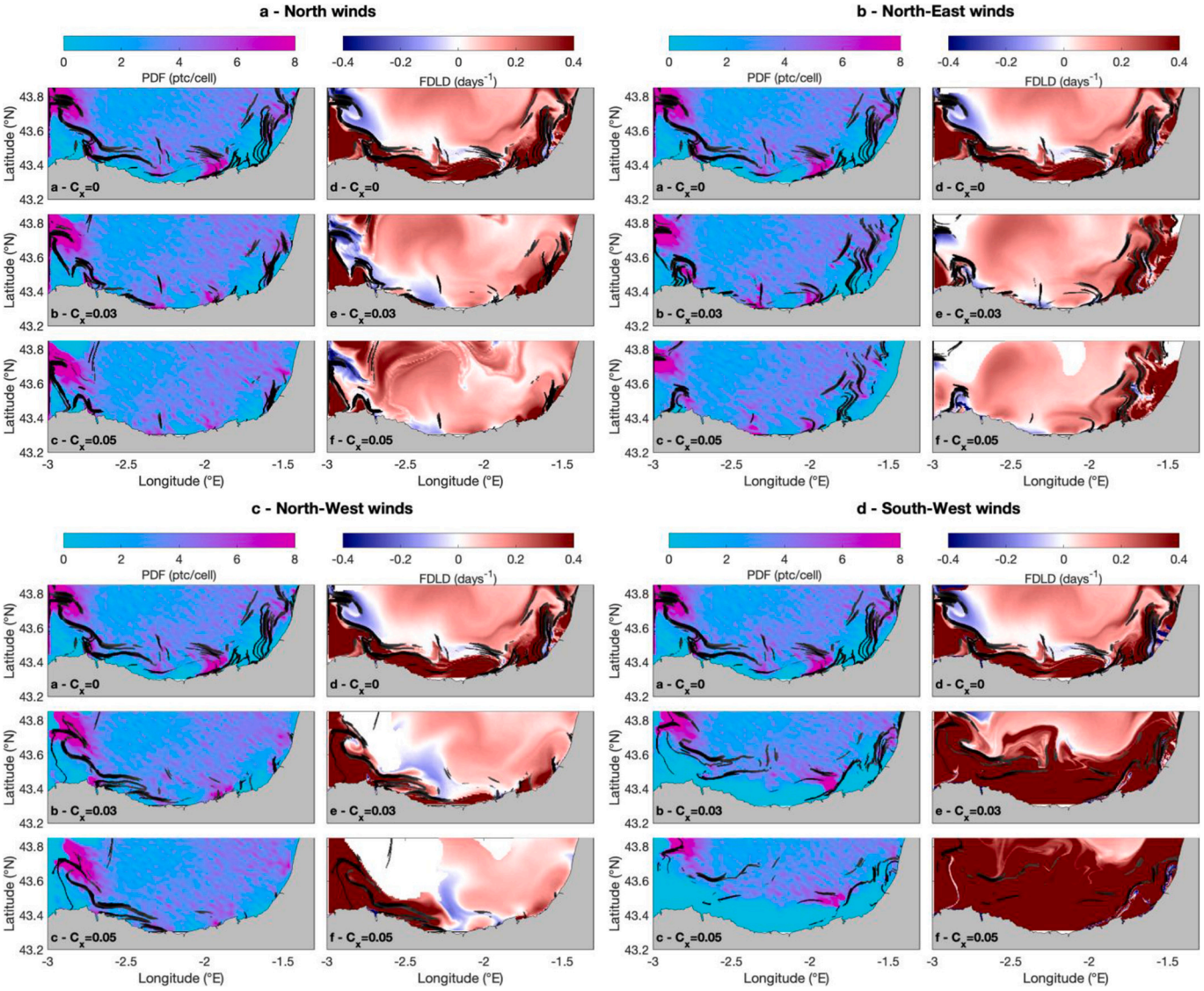

Fig. B5. PDF snapshots on April 28th, 2022, at 03:00 with superimposed FSLE ridgelines (a, b, c) and FDLD snapshots on the same date with superimposed FSLE ridgelines (d, e, f). The FSLE ridgelines have been plotted above the threshold of 0.7. PDF, FDLD and FSLE were computed using theoretical winds: north winds (A), north-east winds (B), north-west winds (C) and south-west winds (D).

Data availability

Data will be made available on request.

References

Allshouse, M.R., Ivey, G.N., Lowe, R.J., Jones, N.L., Beegle-Krause, C.J., Xu, J., Peacock, T., 2017. Impact of windage on ocean surface Lagrangian coherent structures. Environ. Fluid Mech. 17, 473–483. https://doi.org/10.1007/s10652-016-9499-3.

Ardhuin, F., Marié, L., Rascle, N., Forget, P., Roland, A., 2009. Observation and estimation of lagrangian, stokes, and Eulerian currents induced by wind and waves at the sea surface. J. Phys. Oceanogr. 39, 2820–2838. https://doi.org/10.1175/2009JPO4169.1.

Ardhuin, F., Roland, A., Dumas, F., Bennis, A.-C., Sentchev, A., Forget, P., Wolf, J., Girard, F., Osuna, P., Benoit, M., 2012. Numerical wave modeling in conditions with strong currents: dissipation, refraction, and relative wind. J. Phys. Oceanogr. 42, 2101–2120. https://doi.org/10.1175/JPO-D-11-0220.1.

Ardhuin, F., Aksenov, Y., Benetazzo, A., Bertino, L., Brandt, P., Caubet, E., Chapron, B., Collard, F., Cravatte, S., Delouis, J.-M., Dias, F., Dibarboure, G., Gaultier, L., Johannessen, J., Korosov, A., Manucharyan, G., Menemenlis, D., Menendez, M., Monnier, G., Mouche, A., Nouguier, F., Nurser, G., Rampal, P., Reniers, A., Rodriguez, E., Stopa, J., Tison, C., Ubelmann, C., van Sebille, E., Xie, J., 2018. Measuring currents, ice drift, and waves from space: the sea surface KInematics multiscale monitoring (SKIM) concept. Ocean Sci. 14, 337–354. https://doi.org/10.5194/os-14-337-2018.

Aurell, E., Boffetta, G., Crisanti, A., Paladin, G., Vulpiani, A., 1997. Predictability in the large: an extension of the concept of Lyapunov exponent. J. Phys. A Math. Gen. 30, 1. https://doi.org/10.1088/0305-4470/30/1/003.

Ayouche, A., Carton, X., Charria, G., Theettens, S., Ayoub, N., 2020. Instabilities and vertical mixing in river plumes: application to the Bay of Biscay. Geophysical & Astrophysical Fluid Dynamics 114, 650–689. https://doi.org/10.1080/03091929.2020.1814275.

Berti, S., Alves Dos Santos, F., Lacorata, G., Vulpiani, A., 2011. Lagrangian drifter dispersion in the southwestern Atlantic Ocean. J. Phys. Oceanogr. 41, 1659–1672. https://doi.org/10.1175/2011JPO4541.1.

Bertin, S., Rubio, A., Hernández-Carrasco, I., Solabarrieta, L., Ruiz, I., Orfila, A., Sentchev, A., 2024a. Coastal current convergence structures in the Bay of Biscay from optimized high-frequency radar and satellite data. Sci. Total Environ. 947, 174372. https://doi.org/10.1016/j.scitotenv.2024.174372.

Bertin, S., Sentchev, A., Alekseenko, E., 2024b. Fusion of Lagrangian drifter data and numerical model outputs for improved assessment of turbulent dispersion. Ocean Sci. 20, 965–980. https://doi.org/10.5194/os-20-965-2024.

Bettencourt, J.H., López, C., Hernández-García, E., 2013. Characterization of coherent structures in three-dimensional turbulent flows using the finite-size Lyapunov exponent. J. Phys. A Math. Theor. 46, 254022. https://doi.org/10.1088/1751-8113/46/25/254022.

Bouzaiene, M., Menna, M., Poulain, P.-M., Bussani, A., Elhmaidi, D., 2020. Analysis of the surface dispersion in the Mediterranean sub-basins. Front. Mar. Sci. 7.

Breivik, Ø., Allen, A.A., Maisondieu, C., Roth, J.C., 2011. Wind-induced drift of objects at sea: the leeway field method. Appl. Ocean Res. 33, 100–109. https://doi.org/10.1016/j.apor.2011.01.005.
Capó, E., McWilliams, J.C., Mason, E., Orfila, A., 2021. Intermittent frontogenesis in the Alboran Sea. J. Phys. Oceanogr. https://doi.org/10.1175/JPO-D-20-0277.1.
Charria, G., Lazure, P., Le Cann, B., Serpette, A., Reverdin, G., Louazel, S., Batifoulier, F., Dumas, F., Pichon, A., Morel, Y., 2013. Surface layer circulation derived from Lagrangian drifters in the Bay of Biscay. Journal of Marine Systems, XII International Symposium on Oceanography of the Bay of Biscay 109. https://doi.org/10.1016/j.jmarsys.2011.09.015. S60–S76.
Chavanne, C., 2018. Do high-frequency radars measure the wave-induced Stokes drift? J. Atmos. Ocean. Technol. https://doi.org/10.1175/JTECH-D-17-0099.1.
Cózar, A., Echevarría, F., González-Gordillo, J.I., Irigoien, X., Úbeda, B., Hernández-León, S., Palma, Á.T., Navarro, S., García-de-Lomas, J., Ruiz, A., Fernández-de-Puelles, M.L., Duarte, C.M., 2014. Plastic debris in the open ocean. Proc. Natl. Acad. Sci. 111, 10239–10244. https://doi.org/10.1073/pnas.1314705111.
Curcic, M., Chen, S.S., Özgökmen, T.M., 2016. Hurricane-Induced Ocean waves and stokes drift and their impacts on surface transport and dispersion in the Gulf of Mexico. Geophys. Res. Lett. 43, 2773–2781. https://doi.org/10.1002/2015GL067619.
D'Asaro, Shcherbina, A., Klymak, J., Molemaker, J., Novelli, G., Guigand, C., Haza, A., Haus, B., Ryan, E., Jacobs, G., Huntley, H., Laxague, N., Chen, S., Judt, F., McWilliams, J., Barkan, R., Kirwan, A., Poje, A., Özgökmen, T., 2018. Ocean convergence and the dispersion of flotsam. Proc. Natl. Acad. Sci. 115, 201718453. https://doi.org/10.1073/pnas.1718453115.
Davila, X., Rubio, A., Artigas, L.F., Puillat, I., Manso-Narvarte, I., Lazure, P., Caballero, A., 2021. Coastal submesoscale processes and their effect on phytoplankton distribution in the southeastern Bay of Biscay. Ocean Sci. 17, 849–870. https://doi.org/10.5194/os-17-849-2021.
Davis, R.E., 1983. Oceanic property transport, Lagrangian particle statistics, and their prediction. J. Mar. Res. 41, 163–194.
de Mello, C., Barreiro, M., Hernandez-Garcia, E., Trinchin, R., Manta, G., 2023. A Lagrangian study of summer upwelling along the Uruguayan coast. Cont. Shelf Res. 258, 104987. https://doi.org/10.1016/j.csr.2023.104987.
Declerck, A., Delpey, M., Rubio, A., Ferrer, L., Basurko, O.C., Mader, J., Louzao, M., 2019. Transport of floating marine litter in the coastal area of the South-Eastern Bay of Biscay: a Lagrangian approach using modelling and observations. J. Oper. Oceanogr. 12, S111–S125. https://doi.org/10.1080/1755876X.2019.1611708.
Dobler, D., Huck, T., Maes, C., Grima, N., Blanke, B., Martinez, E., Ardhuin, F., 2019. Large impact of stokes drift on the fate of surface floating debris in the south Indian Basin. Mar. Pollut. Bull. 148, 202–209. https://doi.org/10.1016/j.marpolbul.2019.07.057.
d'Ovidio, F., Fernández, V., Hernández-García, E., López, C., 2004. Mixing structures in the Mediterranean Sea from finite-size Lyapunov exponents. Geophys. Res. Lett. 31. https://doi.org/10.1029/2004GL020328.
Dussol, A., Chavanne, C., Gregorio, S., Dumont, D., 2022. Experimental confirmation of Stokes drift measurement by high-frequency radars. J. Atmos. Ocean. Technol. https://doi.org/10.1175/JTECH-D-21-0025.1.
Enrile, F., Besio, G., Stocchino, A., Magaldi, M.G., 2019. Influence of initial conditions on absolute and relative dispersion in semi-enclosed basins. PLoS One 14, e0217073. https://doi.org/10.1371/journal.pone.0217073.
Essink, S., 2019. Lagrangian Dispersion and Deformation in Submesoscale Flows. Institute of Technology, Massachusetts.
Ferrer, L., Fontán, A., Mader, J., Chust, G., González, M., Valencia, V., Uriarte, Ad., Collins, M.B., 2009. Low-salinity plumes in the oceanic region of the Basque Country. Continental Shelf Research, 100 Years of Research within the Bay of Biscay. Cont. Shelf Res. 29, 970–984. https://doi.org/10.1016/j.csr.2008.12.014.
Fontán, A., González, M., Wells, N., Collins, M., Mader, J., Ferrer, L., Esnaola, G., Uriarte, A., 2009. Tidal and wind-induced circulation within the southeastern limit of the Bay of Biscay: Pasaia Bay, Basque coast. Cont. Shelf Res. 29, 998–1007. https://doi.org/10.1016/j.csr.2008.12.013.
González, M., Uriarte, A., Fontán, A., Mader, J., Gyssels, P., 2004. Oceanography. Marine environment. Basque Country. In: Marine Dynamics, pp. 133–157.
Gove, J.M., Whitney, J.L., McManus, M.A., Lecky, J., Carvalho, F.C., Lynch, J.M., Li, J., Neubauer, P., Smith, K.A., Phipps, J.E., Kobayashi, D.R., Balagso, K.B., Contreras, E. A., Manuel, M.E., Merrifield, M.A., Polovina, J.J., Asner, G.P., Maynard, J.A., Williams, G.J., 2019. Prey-size plastics are invading larval fish nurseries. Proc. Natl. Acad. Sci. 116, 24143–24149. https://doi.org/10.1073/pnas.1907496116.
Haller, G., 2015. Lagrangian coherent structures. Annu. Rev. Fluid Mech. 47, 137–162. https://doi.org/10.1146/annurev-fluid-010313-141322.
Haza, A.C., Poje, A.C., Özgökmen, T.M., Martin, P., 2008. Relative dispersion from a high-resolution coastal model of the Adriatic Sea. Ocean Model 22, 48–65. https://doi.org/10.1016/j.ocemod.2008.01.006.
Hernández-Carrasco, Ismael, López, Cristóbal, Hernández-García, Emilio, Turiel, Antonio, 2011. How reliable are finite-size Lyapunov exponents for the assessment of ocean dynamics? Ocean Modelling 36 (3–4), 208–218. https://doi.org/10.1016/j.ocemod.2010.12.006. ISSN 1463-5003.
Hernández-Carrasco, I., Orfila, A., 2018. The role of an intense front on the connectivity of the Western Mediterranean Sea: the Cartagena-Tenes front. J. Geophys. Res. Oceans 123, 4398–4422. https://doi.org/10.1029/2017JC013613.
Hernández-Carrasco, I., Orfila, A., Rossi, V., Garçon, V., 2018. Effect of small scale transport processes on phytoplankton distribution in coastal seas. Sci. Rep. 8, 8613. https://doi.org/10.1038/s41598-018-26857-9.
Hernández-Carrasco, I., Alou-Font, E., Dumont, P.-A., Cabornero, A., Allen, J., Orfila, A., 2020. Lagrangian flow effects on phytoplankton abundance and composition along filament-like structures. Prog. Oceanogr. 189, 102469. https://doi.org/10.1016/j.pocean.2020.102469.
Hernández-Carrasco, I., Rossi, V., Navarro, G., Turiel, A., Bracco, A., Orfila, A., 2023. Flow structures with high Lagrangian coherence rate promote diatom blooms in oligotrophic waters. Geophys. Res. Lett. 50. https://doi.org/10.1029/2023GL103688.
Hernández-Lasheras, J., Orfila, A., Santana, A., Hernández-Carrasco, I., Mourre, B., 2025. High frequency radar observing system simulation experiment in the Western Mediterranean Sea. A Lagrangian assessment approach. Ocean Model 196, 102553. https://doi.org/10.1016/j.ocemod.2025.102553.
Hodgins, D.O., Hodgins, S.L., 1998. Phase II Leeway Dynamics Program: Development and Verification of a Mathematical Drift Model for Liferafts and Small Boats. Seaconsult Marine Research Limited.
Huntley, H.S., Lipphardt Jr., B.L., Jacobs, G., Kirwan Jr., A.D., 2015. Clusters, deformation, and dilation: diagnostics for material accumulation regions. J. Geophys. Res. Oceans 120, 6622–6636. https://doi.org/10.1002/2015JC011036.
Jones, C.E., Dagestad, K.-F., Breivik, Ø., Holt, B., Röhrs, J., Christensen, K.H., Espeseth, M., Brekke, C., Skrunes, S., 2016. Measurement and modeling of oil slick transport. J. Geophys. Res. Oceans 121, 7759–7775. https://doi.org/10.1002/2016JC012113.
Kohonen, T., 1998. The self-organizing map. Neurocomputing 21, 1–6. https://doi.org/10.1016/S0925-2312(98)00030-7.
Kumar, J., Choudhary, R.K., Mathur, M., Agarwal, N., Sharma, R., 2023. A study of mixing and biological activity in the North Indian Ocean using finite size Lyapunov exponents. J Indian Soc Remote Sens 51, 395–403. https://doi.org/10.1007/s12524-022-01564-1.
LaCasce, J.H., 2008. Statistics from Lagrangian observations. Prog. Oceanogr. 77, 1–29.
Le Cann, B., 1990. Barotropic tidal dynamics of the Bay of Biscay shelf: observations, numerical modelling and physical interpretation. Cont. Shelf Res. 10, 723–758. https://doi.org/10.1016/0278-4343(90)90008-A.
Liu, Y., Weisberg, R.H., Mooers, C.N.K., 2006. Performance evaluation of the self-organizing map for feature extraction. J. Geophys. Res. Oceans 111. https://doi.org/10.1029/2005JC003117.
Lobelle, D., Kooi, M., Koelmans, A.A., Laufkötter, C., Jongedijk, C.E., Kehl, C., van Sebille, E., 2021. Global modeled sinking characteristics of biofouled microplastic. J. Geophys. Res. Oceans 126. https://doi.org/10.1029/2020JC017098 e2020JC017098.
Mann, K.H., Lazier, J.R., 2005. Dynamics of Marine Ecosystems: Biological-Physical Interactions in the Oceans. John Wiley & Sons.
Mantovani, C., Corgnati, L., Horstmann, J., Rubio, A., Reyes, E., Quentin, C., Cosoli, S., Asensio, J.L., Mader, J., Griffa, A., 2020. Best practices on high frequency radar deployment and operation for ocean current measurement. Front. Mar. Sci. 7.
McWilliams, J.C., 2016. Submesoscale currents in the ocean. Proceedings of the Royal Society A: Mathematical, Physical and Engineering Sciences 472, 20160117. https://doi.org/10.1098/rspa.2016.0117.
Mei, C.C., 1989. The Applied Dynamics of Ocean Surface Waves. World scientific.
Morales Márquez, V., Hernández-Carrasco, I., Simarro, G., Rossi, V., Orfila, A., 2021. Regionalizing the impacts of wind- and wave-induced currents on Surface Ocean dynamics: a long-term variability analysis in the Mediterranean Sea. J. Geophys. Res. Oceans 126. https://doi.org/10.1029/2020JC017104.
Morales Márquez, V., Hernández-Carrasco, I., Fox-Kemper, B., Orfila, A., 2023. Ageostrophic contribution by the wind and waves induced flow to the lateral stirring in the Mediterranean Sea. J. Geophys. Res. Oceans 128. https://doi.org/10.1029/2022JC019135.
Nencioli, F., d'Ovidio, F., Doglioli, A.M., Petrenko, A.A., 2011. Surface coastal circulation patterns by in-situ detection of Lagrangian coherent structures. Geophys. Res. Lett. 38. https://doi.org/10.1029/2011GL048815.
Orfila, A., Urbano-Latorre, C.P., Sayol, J.M., Gonzalez-Montes, S., Caceres-Euse, A., Hernández-Carrasco, I., Muñoz, Á.G., 2021. On the impact of the Caribbean counter current in the Guajira upwelling system. Front. Mar. Sci. 8. https://doi.org/10.3389/fmars.2021.626823.
Park, Y.-G., Seo, S., 2021. Review on Lagrangian particle tracking modeling for floating objects around the Korean peninsula. KMI International Journal of Maritime Affairs and Fisheries 13, 67–83. https://doi.org/10.54007/ijmaf.2021.13.2.67.
Pereiro, D., Souto, C., Gago, J., 2019. Dynamics of floating marine debris in the northern Iberian waters: a model approach. J. Sea Res. 144, 57–66. https://doi.org/10.1016/j.seares.2018.11.007.
Pingree, R.D., Le Cann, B., 1992. Three anticyclonic slope water oceanic eDDIES (SWODDIES) in the southern Bay of Biscay in 1990. Deep Sea Res. Part A 39, 1147–1175. https://doi.org/10.1016/0198-0149(92)90062-X.
Poje, A.C., Özgökmen, T.M., Lipphardt, B.L., Haus, B.K., Ryan, E.H., Haza, A.C., Jacobs, G.A., Reniers, A.J.H.M., Olascoaga, M.J., Novelli, G., Griffa, A., Beron-Vera, F.J., Chen, S.S., Coelho, E., Hogan, P.J., Kirwan, A.D., Huntley, H.S., Mariano, A.J., 2014. Submesoscale dispersion in the vicinity of the Deepwater horizon spill. Proc. Natl. Acad. Sci. 111, 12693–12698. https://doi.org/10.1073/pnas.1402452111.
Poulain, P.-M., Niiler, P.P., 1989. Statistical analysis of the surface circulation in the California current system using satellite-tracked drifters. J. Phys. Oceanogr. 19, 1588–1603. https://doi.org/10.1175/1520-0485(1989)019<1588:SAOTSC>2.0.CO;2.
Reverdin, G., Marié, L., Lazure, P., d'Ovidio, F., Boutin, J., Testor, P., Martin, N., Lourenco, A., Gaillard, F., Lavin, A., Rodriguez, C., Somavilla, R., Mader, J., Rubio, A., Blouch, P., Rolland, J., Bozec, Y., Charria, G., Batifoulier, F., Dumas, F., Louazel, S., Chanut, J., 2013. Freshwater from the Bay of Biscay shelves in 2009. Journal of Marine Systems, XII International Symposium on Oceanography of the

Bay of Biscay 109–110, S134–S143. https://doi.org/10.1016/j.jmarsys.2011.09.017.
Rodríguez-Díaz, L., Gómez-Gesteira, J.L., Costoya, X., Gómez-Gesteira, M., Gago, J., 2020. The Bay of Biscay as a trapping zone for exogenous plastics of different sizes. J. Sea Res. 163, 101929. https://doi.org/10.1016/j.seares.2020.101929.
Röhrs, J., Sperrevik, A.K., Christensen, K.H., Broström, G., Breivik, Ø., 2015. Comparison of HF radar measurements with Eulerian and Lagrangian surface currents. Ocean Dyn. 65, 679–690. https://doi.org/10.1007/s10236-015-0828-8.
Rubio, A., Reverdin, G., Fontán, A., González, M., Mader, J., 2011. Mapping near-inertial variability in the SE Bay of Biscay from HF radar data and two offshore moored buoys. Geophys. Res. Lett. 38. https://doi.org/10.1029/2011GL048783.
Rubio, A., Caballero, A., Orfila, A., Hernández-Carrasco, I., Ferrer, L., González, M., Solabarrieta, L., Mader, J., 2018. Eddy-induced cross-shelf export of high Chl-a coastal waters in the SE Bay of Biscay. Remote Sens. Environ. 205, 290–304. https://doi.org/10.1016/j.rse.2017.10.037.
Rubio, A., Manso-Narvarte, I., Caballero, A., Corgnati, L., Mantovani, C., Reyes, E., Griffa, A., Mader, J., 2019. The Seasonal Intensification of the Slope Iberian Poleward Current.
Rubio, A., Hernández-Carrasco, I., Orfila, A., González, M., Reyes, E., Corgnati, L., Berta, M., Griffa, A., Mader, J., 2020. A Lagrangian approach to monitor local particle retention conditions in coastal areas. Copernicus Marine Service Ocean State Report 54–59.
Ruiz, I., Basurko, O.C., Rubio, A., Delpey, M., Granado, I., Declerck, A., Mader, J., Cózar, A., 2020. Litter windrows in the South-East Coast of the Bay of Biscay: an ocean process enabling effective active fishing for litter. Front. Mar. Sci. 7.
Ruiz, I., Abascal, A.J., Basurko, O.C., Rubio, A., 2022. Modelling the distribution of fishing-related floating marine litter within the Bay of Biscay and its marine protected areas. Environ. Pollut. 292, 118216. https://doi.org/10.1016/j.envpol.2021.118216.
Sainte-Rose, B., Lebreton, L., Rego, J., Kleissen, F., Reisser, J., 2016. Multi-Scale Numerical Analysis of the Field Efficiency of an Ocean Plastic Cleanup Array. https://doi.org/10.1115/OMAE2016-54926.
Siegelman, L., Klein, P., Thompson, A.F., Torres, H.S., Menemenlis, D., 2020. Altimetry-based diagnosis of deep-reaching sub-Mesoscale Ocean fronts. Fluids 5, 145. https://doi.org/10.3390/fluids5030145.
Skamarock, W.C., Klemp, J.B., Dudhia, J., Gill, D.O., Liu, Z., Berner, J., Wang, W., Powers, J.G., Duda, M.G., Barker, D.M., 2019. A description of the advanced research WRF version 4. In: NCAR tech. Note NCAR/tn-556+ str, p. 145.
Solabarrieta, L., Rubio, A., Castanedo, S., Medina, R., Charria, G., Hernández, C., 2014. Surface water circulation patterns in the southeastern Bay of Biscay: new evidences from HF radar data. Cont. Shelf Res. 74, 60–76. https://doi.org/10.1016/j.csr.2013.11.022.
Solabarrieta, L., Rubio, A., Cárdenas, M., Castanedo, S., Esnaola, G., Méndez, F.J., Medina, R., Ferrer, L., 2015. Probabilistic relationships between wind and surface water circulation patterns in the SE Bay of Biscay. Ocean Dyn. 65, 1289–1303. https://doi.org/10.1007/s10236-015-0871-5.
Solabarrieta, L., Frolov, S., Cook, M., Paduan, J., Rubio, A., González, M., Mader, J., Charria, G., 2016. Skill assessment of HF radar–derived products for Lagrangian simulations in the Bay of Biscay. J. Atmos. Ocean. Technol. 33, 2585–2597. https://doi.org/10.1175/JTECH-D-16-0045.1.
Taani, A., Abushattal, A., Mardini, M.K., 2019. The regular dynamics through the finite-time Lyapunov exponent distributions in 3D Hamiltonian systems. Astronomische Nachrichten 340, 847–851. https://doi.org/10.1002/asna.201913713.
Taylor, G.I., 1922. Diffusion by continuous movements. Proc. Lond. Math. Soc. 2, 196–212.
Tran, M.C., Sentchev, A., Berti, S., Ayoub, N.K., Nguyen-Duy, T., Cuong, N.K., 2022. Assessment of relative dispersion in the Gulf of Tonkin using numerical modeling and HF radar observations of surface currents. Cont. Shelf Res. 245, 104784. https://doi.org/10.1016/j.csr.2022.104784.
Valencia, V., Franco, J., Borja, A., Fontán, A., 2004. Hydrography of the southeastern Bay of Biscay. Oceanography and Marine Environment of the Basque Country. 159–194. https://doi.org/10.1016/S0422-9894(04)80045-X.
van den Bremer, T.S., Breivik, Ø., 2018. Stokes drift. Philos. Trans. R. Soc. A Math. Phys. Eng. Sci. 376, 20170104. https://doi.org/10.1098/rsta.2017.0104.
Vandermeirsch, F., Bonnat, A., Yin, X., Lazure, P., 2012. Courantologie. Sous-région marine Golfe de Gascogne. Evaluation initiale DCSMM, MEDDE, AAMP, Ifremer, Ref.
Vatanen, T., Osmala, M., Raiko, T., Lagus, K., Sysi-Aho, M., Orešič, M., Honkela, T., Lähdesmäki, H., 2015. Self-organization and missing values in SOM and GTM. Neurocomputing 147, 60–70. https://doi.org/10.1016/j.neucom.2014.02.061. ISSN 0925-2312.
Veatch, J., Fredj, E., Kohut, J., 2022. High frequency radars as ecological sensors: Using Lagrangian coherent structures to quantify prey concentrating features. In: OCEANS 2022, Hampton Roads. Presented at the OCEANS 2022, Hampton Roads, pp. 1–7. https://doi.org/10.1109/OCEANS47191.2022.9977356.
Yaremchuk, M., Sentchev, A., 2009. Mapping radar-derived sea surface currents with a variational method. Cont. Shelf Res. 29, 1711–1722. https://doi.org/10.1016/j.csr.2009.05.016.
Yoon, J.-H., Kawano, S., Igawa, S., 2009. Modeling of marine litter drift and beaching in the Japan Sea. Mar. Pollut. Bull. 60, 448–463. https://doi.org/10.1016/j.marpolbul.2009.09.033.
Zhang, H., 2017. Transport of microplastics in coastal seas. Estuar. Coast. Shelf Sci. 199, 74–86. https://doi.org/10.1016/j.ecss.2017.09.032.